# An empirical study of the correlation between the Hall and Pedersen ionospheric conductivities and the field-aligned currents at high latitudes.

Espen Skjerlie Simonsen

Thesis for degree of Master of Science
Space Physics


University of Bergen, Norway
Department of Physics and Technology
2019

# Preface

I would like to start with expressing my sincerest gratitude to the Birkeland Centre for Space Science for the opportunity to do my thesis for a degree in Master of Science, at the Department of Physics and technology, University of Bergen (Norway). I would like to thank my supervisor Therese Moretto Jørgensen. Her patience and encouragement has made working on this thesis a joyous endeavour. I would also like to give a special thanks to Spencer Mark Hatch, who has gone to great lengths to aid and assist me in overcoming whatever challenges I encountered. Their knowledge of space physics and willingness to share has served as an inspiration. I want to thank everyone at the Birkeland Centre for creating a welcoming work environment, and an extra thank goes to all my fellow master students; Ingrid, Josephine, Tage, Andreas, Amalie, Jone, Judit and Ragnar. Their optimism and high spirit created a very positive environment that made me look forward to every day at the office. Finally I would like to thank my parents; May Kristin Skjerlie and Egil Simonsen, and my brother Aleksander Skjerlie Simonsen for putting faith in me, and for their continued support and encouragement throughout my education.

Bergen, October 2019

# Contents

# List of Figures

# Nomenclature

**Abbreviations**

AMPERE Active Magnetosphere and Planetary Electrodynamics Response Experiment

EISCAT European Incoherent SCATter

FAC Field-Aligned Current

IMF Interplanetary Magnetic Field

MHD Magneto Hydro Dynamics

MLT Magnetic Local Time

PFISR Poker Flat Incoherent Scatter Radar

UTC Coordinated Universal Time

**Constants**

$\epsilon_0$ $8.85419 \times 10^{-12}\,\mathrm{Fm}^{-1}$ Permittivity of free space

$\mu_0$ $1.25664 \times 10^{-6}\,\mathrm{Hm}^{-1}$ Permeability of free space

$e$ $1.60218 \times 10^{-19}$ C Elementary Charge

$k_B$ $1.3806 \times 10^{-23}\,\mathrm{m}^{-2}\mathrm{kgs}^{-2}\mathrm{K}^{-1}$ Boltzmann's constant

$m_e$ $9.10938 \times 10^{-31}$ kg Electron mass

# Chapter 1

# Introduction to the thesis

Ever since man settled in the polar regions of our planet, we have been aware of the auroras. In a multitude of primitive mythologies and religions, from China to Finland, Greece and ancient Rome and to the native Americans, the auroras are a metaphysical phenomenon with varying degrees of significance. To the Chinese it was believed to be signs of mythical wars raging across the night-sky. In Finland it was believed to be the trail of a fox running so fast across the sky its tail would make sparks that left a blazing trail [1]. The Cree Indians believed it to be the ghosts and spirits of their ancestors dancing in the heavens [2]. For thousands of years these strange lights would go unexplained. When the age of enlightenment began and the first footholds of modern scientific theory was established, work began to understand the auroras. Initially the auroras was believed to influence the weather, and British astronomer Edmond Halley believed it to be caused by a magnetic fluid leaking from the Earth [3]. By the end of the 19th century, we knew the auroras was not a reflection, but rather originated from the atmosphere. We knew that it was most common in a circle roughly 2500 kilometers from the pole, at a height that was variously estimated to be as high as 1000 kilometers and as low as ground level. In 1896 Norwegian physicist Kristian Birkeland succeeded in creating light that resembled the auroras in the vicinity of a magnet when attracting cathode rays [4]. From this he would formulate his hypothesis that the auroras must be created by cathode rays, with the sun as the likely source [5]. On November 1. 1899 he began his observations of the auroras from Haldenposten outside Alta, Norway. Here he would correctly measure the aurora height to approximately 100 kilometers above ground, and found that auroras was always accompanied by geomagnetic disturbances [6]. After these observations he returned to Christiania to create the terella experiment which recreated auroras around a magnetized metal sphere. It was not until the 1960's, when mankind launched satellites beyond the Earth's magnetosphere that his was research confirmed, when American and Soviet probes detected what would later be recognized as the solar wind [7].

Extensive work has been done since then to piece together a complete understanding of the coupling between the sun, the magnetosphere and the ionosphere of the Earth. The launch of multiple satellites and the construction of radars and observatories, have confirmed the existence of currents flowing in and out of the ionosphere, that are now known as Birkeland currents. In 1961 James Wynne Dungey proposed that reconnection between the interplanetary magnetic field (IMF) and the magnetic field of Earth drove the plasma convection within the Earth's magnetosphere [8]. Before then Hannes Alfvén's model of magnetichydrodynamics (MHD) had been proposed [9], for which he received the Nobel prize in physics in 1970. The study of MHD would allow modeling of plasma behaviour in the solar wind and within the magnetosphere. These models continue to be studied today in greater detail, but the entirety of the system is yet to be completely understood.

One field of interest in magnetosphere-ionosphere coupling is how changes in conditions of one system might affect the other. The ionosphere allows magnetospheric currents to close, thereby allowing magnetospheric convection to occur. The transport of plasma in the ionosphere is expected to change the ion and electron profiles. In 1972 Knight established mathematically that a relationship between the upward field aligned current regions and the energy of precipitating electrons exist [10]. In 1991 the relationship between precipitating electrons and local height integrated conductance was empirically shown (Robinson et al [11] , Lumerzheim et al 1991 [12]). The logical path of these relationships would then become the relationship between the field-aligned currents(FAC) and local height integrated conductance (Ridley at al 2002 [13]) which was later shown empirically (Robinson 2019 [14]). Robinson found that there is a correlation between strong field aligned currents and conductance for both upward and downward currents, but mainly on the night-side. The Poker Flat Incoherent scatter radar (PFSIR) was used in these experiments to find the local conductance, while the Active Magnetosphere and Planetary Electrodynamics Response Experiment (AMPERE) communications satellite constellation was used to derive the FACs. In Robinson, 2019 other research institutes are encouraged do similar studies from other high-latitude incoherent scatter radar sites such as Svalbard and Tromsø to study the geomagnetic dependencies in the statistical relation between FAC and conductances. In this thesis the same study is conducted using the European Incoherent SCATter Radar (EISCAT) at Svalbard (Norway).

An incoherent scatter radar functions by shooting rapid radar pulses which are then scattered by the electrons and ions in the ionosphere. This incoherent scatter return allows for measurements of the electron density, ion and electron temperature as well as ion composition. These measurements in turn allow for estimation of the conductivity, which is integrated over height to get the conductance [15]. The field aligned currents are derived

by applying Ampére's law to the magnetic perturbations caused by the magnetic field disturbances [17].

In Chapter 2 of this thesis, an introduction to the principles behind MHD is given and how this is applied to the magnetosphere to explain the transport of plasma and generation of associated currents. The basic properties of the ionosphere and the conductance is also provided. In Chapter 3 the data derived from the EISCAT and AMPERE experiments is laid out in detail. How these data are processed and used in our study is provided in detail. Chapter 4 presents the results of the data comparison and analysis, with further comments and conclusion in Chapter 5. Chapter 6 summarizes the conclusions of the thesis and gives an outlook for future work.

# Chapter 2

# Theory

In this chapter a short introduction to the magnetosphere-ionosphere system is given. The basics of magnetohydrodynamics (MHD) is presented [18], and it is shown how these equations explain how convection in the magneto-tail achieves currents and convection in the ionosphere through field-aligned currents. The principles of plasma conductivity are stated, and the Hall and Pedersen conductivities presented.

## 2.1 Magnetohydrodynamics.

In order to get a comprehensive picture of how the magnetosphere-ionosphere system behaves, an introduction into MHD is given.

MHD is a model in which plasma is described as an in-compressible fluid rather than individually moving particles. This model allows for large scale modelling that would ordinarily be to complex to solve. MHD works primarily for large plasma systems. A short description of how one arrives at the governing equations for MHD is given here.

### 2.1.1 Single particle physics

Assume that there exist some large collection of charged particles. If one is to describe this collection the state of the system must be known, and equations for its evolution are required. Assuming that some function F exist that would describe the particle collection exactly, $\frac{dF}{dt}$ would be its natural time evolution.

To describe F exactly, phase space is introduced for convenience. Phase space is an imaginary six-dimensional space where all Eulerian coordinates for a given particles position and

velocity are represented uniquely. To guarantee exact coordinates in both position space and velocity space, each particle is defined by a delta-Dirac function. To get the entirety of the population, F will sum up over all the particles producing the equation:

$$F_m(\mathbf{x},\mathbf{v},t) = \sum_{i=1}^{N} \delta[\mathbf{x} - \mathbf{x}_i(t)]\delta[\mathbf{v} - \mathbf{v}_i(t)] \tag{2.1}$$

Where $\mathbf{x} = (x, y, z)$ and $\mathbf{v} = (v_x, v_y, v_z)$. This is the equation of state for exact particle location and particle velocity. If F is integrated over both velocity space $dv$ and position space $dx$, the total number of particles N would be found. If F is integrated only over velocity space the number density $n(x, t)$ is produced.

$$\int F_m(\mathbf{x},\mathbf{v},t)dv = n_m(\mathbf{x},t) \tag{2.2}$$

Now that the equation of state is given, its evolution can be explored.

If the total derivative $\frac{dF}{dt}$ is taken, its partial derivatives will need to be presented. This can be written as $\frac{dF}{dt} = \frac{\partial F}{\partial t} + \frac{\partial F}{\partial x}\frac{\partial x}{\partial t} + \frac{\partial F}{\partial v}\frac{\partial v}{\partial t}$. The evolution of each particle will be determined by the forces acting on it by the following equations.

$$\frac{\partial \mathbf{x}_i}{\partial t} = \mathbf{v}_i(t) \tag{2.3}$$

$$\frac{\partial \mathbf{v}_i}{\partial t} = \frac{q_i}{m_i}(\mathbf{E}_m(\mathbf{x}_i(t),t) + \mathbf{v}_i \times \mathbf{B}_m(\mathbf{x}_i(t),t)) \tag{2.4}$$

Equation (2.4) describes the Coloumb force and the Lorentz force acting on a particle. Here, $E_m$ and $B_m$ are the electric and the magnetic fields described by the microscopic Maxwell's equations.

$$\nabla \cdot \mathbf{E}_m = \frac{\rho_c}{\epsilon_o} \tag{2.5a}$$

$$\nabla \cdot \mathbf{B}_m = 0 \tag{2.5b}$$

$$\nabla \times \mathbf{E}_m = -\frac{\partial \mathbf{B}_m}{\partial t} \tag{2.5c}$$

$$\nabla \times \mathbf{B}_m = \mu_0 \mathbf{J}_m + \mu_0 \epsilon_0 \frac{\partial \mathbf{E}_m}{\partial t} \tag{2.5d}$$

Within the Maxwell's equations are charge density and current, given respectively as:

$$\rho_m(\mathbf{x},t) = \sum_s q_s \int \mathbf{F}_s(\mathbf{x},\mathbf{v},t)d\mathbf{v} \tag{2.6a}$$

$$\mathbf{J}_m(\mathbf{x},t) = \sum_s q_s \int \mathbf{F}_s(\mathbf{x},\mathbf{v},t)\mathbf{v}d\mathbf{v} \tag{2.6b}$$

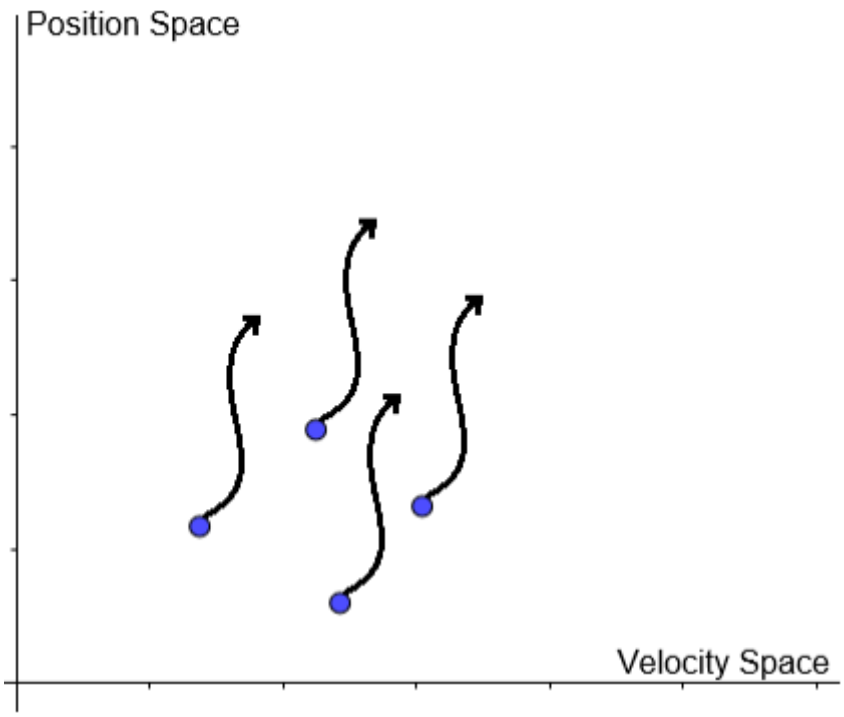


Figure 2.1: Graphic representation of how some given particles evolve in phase space.

If the total derivative is now written out in its completeness, it is as follows:

$$\frac{\partial \mathbf{F}_i}{\partial t} + \mathbf{v}_i \nabla_x \mathbf{F}_i + \frac{q_i}{m_i}(\mathbf{E}_m(\mathbf{x}_i(t), t) + \mathbf{v}_i \times \mathbf{B}_m(\mathbf{x}_i(t), t))\nabla_v \mathbf{F}_i \tag{2.7}$$

Equation (2.7) is the Klimantovich-Dupreè equation, which describes a microscopic set of particles exactly and self-consistently. Within these equations are all the information required to know the evolution of all particles within any stated system.

### 2.1.2 Distribution function.

Although the Klimantovich-Dupreè equation contains all the exact quantities of the microscopic fields, solving it for any large system becomes difficult. It is therefore prudent to seek a simpler way, by averaging over a large number of particles. This averaging assumes that the particles are statistically correlated in time, space and velocity by their interactions.

One can define the ensemble average phase space density as $f(\mathbf{x}, \mathbf{v}, t) = \langle F \rangle(\mathbf{x}, \mathbf{v}, t)$ such that the exact phase space density is the sum of this ensemble average plus some microscopic fluctuations, which accounts for any deviations from the exact to the average. This

can be written as:

$$F(\mathbf{x}, \mathbf{v}, t) = f(\mathbf{x}, \mathbf{v}, t) + \delta F(\mathbf{x}, \mathbf{v}, t) \tag{2.8}$$

The average fluctuations $\langle \delta F \rangle$ would then be 0. Inserting this ensemble average for both the phase space density and the microscopic fields into equation (2.8) and then solving it, yields:

$$\frac{\partial f}{\partial t} + \mathbf{v}\nabla_x f + \frac{q}{m}(\mathbf{E} + \mathbf{v} \times \mathbf{B})\nabla_v f = -\frac{q}{m}\langle \delta\mathbf{E} + \mathbf{v} \times \delta\mathbf{B}) \cdot \nabla_v \delta F \rangle \tag{2.9}$$

This is the kinetic equation of a plasma. The phase space density $f(\mathbf{x}, \mathbf{v}, t)$ is now a coarse grained probability distribution function, and equation (2.9) describes how it evolves under the influence of the average fields. The term on the r.h.s contains all the correlations between the particles and the fields, and solving it is difficult. One way to simplify it is to account for only the correlations between the particles through collisions. This would produce Boltzmann's equation. Since most space plasma however is collision-less, it is far easier to neglect the collision terms entirely.

$$\frac{\partial f}{\partial t} + \mathbf{v}\nabla_x f + \frac{q}{m}(\mathbf{E} + \mathbf{v} \times \mathbf{B})\nabla_v f = 0 \tag{2.10}$$

The above equation is the Vlasov equation, and is the simplest solution to the kinetic equation.

### 2.1.3 Multi-fluid theory

Since the principles governing equation (2.2) is still valid, it is possible to get the ensemble average number density by solving the velocity integral of the distribution function. This yields the macroscopic levels of quantities depending on location and time. If one solves the for the different fluid moments, one gets the following equations:

$$n(\mathbf{x}, t) = \int f(\mathbf{x}, \mathbf{v}, t) d\mathbf{v} \tag{2.11a}$$

$$\mathbf{v}_b(\mathbf{x}, t) = \frac{1}{n} \int \mathbf{v} f(\mathbf{x}, \mathbf{v}, t) d\mathbf{v} \tag{2.11b}$$

$$\Pi(\mathbf{x}, t) = m \int \mathbf{v}\mathbf{v} f(\mathbf{x}, \mathbf{v}, t) d\mathbf{v} \tag{2.11c}$$

These equations yield the number density, bulk flow velocity and the momentum flux density tensor. These quantities are now completely in the macroscopic realm, and any information about individual particles and their behavior is averaged into these quantities.

When solving the different orders of the Vlasov equation, one will find the conservation laws of multi-fluid plasma. The formal solutions to each moment of Vlasov and the sub-

sequent summation of the conservation equations can be found in numerous introduction plasma physics text books. Rather than solving these here, the solutions will simply be shown.

$$\frac{\partial n_s}{\partial t} + \nabla \cdot (n_s \mathbf{v}_s) = 0 \tag{2.12}$$

$$\frac{\partial (n_s \mathbf{v}_s)}{\partial t} + \nabla \cdot (n_s \mathbf{v}_s \mathbf{v}_s) + \frac{1}{m_s} \nabla \cdot \mathbf{P}_s - \frac{q_s}{m_s} n_s (\mathbf{E} + \mathbf{v}_s \times \mathbf{B}) = 0 \tag{2.13}$$

Equation (2.13) is the equation of motion for the given species fluid component. This equation of motion however is not closed, as there is no given expression of the pressure tensor $\mathbf{P}$. To solve this one must calculate the next order of Vlasov, which would result in the Energy equation. This will however produce another higher order quantity, the temperature. This requires solving yet another order of Vlasov and so forth. This is the closure problem. The simplest solution to the closure problem is to make an assumption of the equation of state for the pressure. This renders the Energy equation obsolete, and therefore avoids taking into account the transportation of heat. The most simple equation of state is to assume that the pressure $\mathbf{P}$ behaves like an ideal gas with constant temperature. $\mathbf{P}_s = n_s k_B T_{s0}$. This makes the pressure proportional to the density of the species.

To get to the single-fluid MHD, one will have to sum up the different conservation equations for each species, and multiply with each species-mass respectively. This eliminates all the species dependencies so that only the single fluid terms is present in the MHD equations. Finally, the governing equations for MHD can be given.

$$\frac{\partial \rho}{\partial t} + \nabla \cdot (n \mathbf{v}) = 0 \tag{2.14}$$

$$\frac{\partial (\rho \mathbf{v})}{\partial t} + \nabla \cdot (\rho \mathbf{v} \mathbf{v}) = -\nabla \cdot \mathbf{P} + \mathbf{J} \times \mathbf{B} \tag{2.15}$$

Note that $\rho$ is now our mass density, not to be confused with the charge density $\rho_c$. Equation (2.14) and (2.15) are the continuity equation and momentum conservation equation for a single fluid plasma respectively. Equation (2.15) contains the macroscopic current density term $\mathbf{J}$. To close the set of equation its evolution must be defined. This is found by subtracting the momentum equations for each species from one another, and multiplying each part with its respective species mass. Solving this equation and reducing it to its single fluid terms yields the generalized Ohm's law for single fluid plasma.

$$\mathbf{E} + \mathbf{v} \times \mathbf{B} = \eta \mathbf{J} + \frac{\mathbf{J}}{ne} \times \mathbf{B} - \frac{1}{ne} \nabla \cdot \mathbf{P}_e + \frac{m_e}{ne^2} \frac{\partial \mathbf{J}}{\partial t} \tag{2.16}$$

Here, $\eta$ is the plasma resistivity, and $\mathbf{P}_e$ is the electron pressure. In the solar wind there is negligible electron pressure gradients, near infinite conductivity due to it being collision-less, and weak currents. This also applies to plasma inside the magnetosphere. Applying this to equation (2.16) reduces it to the ideal plasma frozen-in condition $\mathbf{E} = -\mathbf{v} \times \mathbf{B}$. Additional equations to supplement this is Ampére's law and the induction equation (Faraday's law).

$$\nabla \times \mathbf{E} = -\frac{\partial \mathbf{B}}{\partial t} \tag{2.17a}$$

$$\nabla \times \mathbf{B} = \mu_0 \mathbf{J} + \mu_0 \epsilon_0 \frac{\partial \mathbf{E}}{\partial t} \tag{2.17b}$$

The only thing remaining to discuss about MHD is how energy is transferred within the plasma. For that the energy equations for a plasma is given.

$$\frac{\partial}{\partial t}(\frac{\mathbf{B}}{2\mu_0}) + \nabla \cdot \mathbf{S} = -\mathbf{J} \cdot \mathbf{E} \tag{2.18}$$

$$\frac{\partial}{\partial t}(\frac{\rho v^2}{2} + \frac{\mathbf{P}}{\gamma - 1}) + \nabla \cdot (\frac{\rho v^2}{2} + \frac{\gamma \mathbf{P}}{\gamma - 1})\mathbf{v} = \mathbf{J} \cdot \mathbf{E} \tag{2.19}$$

Equation (2.18) describes the magnetic energy stored in the field, while (2.19) describes the kinetic and thermal energy of the plasma. Not that neither of these are a conservation law equalling 0, but rather both equal to the term $\mathbf{J} \cdot \mathbf{E}$. This is because energy is not conserved within each equation, but rather within the system itself. This allows for transport of magnetic energy to kinetic, and vice versa. The vector $\mathbf{S}$ is the Poynting Vector, $\mathbf{S} = \frac{\mathbf{E} \times \mathbf{B}}{\mu_0}$. This vector describes the transport of the magnetic field lines, and is an important vector when looking at how the magnetic field lines are behaving in the Dungey Cycle.

This completes the introduction to MHD. A lot of the equations that are listed here are not properly derived, but rather just stated as is. Their complete and formal definitions are found in the multiple sources of this thesis. Being armed with the defining equations of MHD, the Dungey cycle can now be explored. For the rest of this section, the above equations will be utilized to describe the motion of the magnetic field lines within Earth's magnetosphere, and the subsequent currents this gives rise to.

## 2.2 The Magnetosphere-Ionosphere system.

### 2.2.1 The Solar wind and the Earth's magnetic field

Sunlight is not the only thing radiating from the sun. It is also casting off a constant stream of plasma called the solar wind. This plasma is released from the suns upper atmosphere, the corona. The solar wind consists primarily of electrons, protons and a small fraction of heavier ions. When it reaches Earth it has a velocity somewhere between 200 km/s and 800km/s, with a calm average of 400km/s. The particle density varies from 1 particle per cubic centimeter to 20 particles per cubic centimeter. During extraordinary events such as Coronal Mass Ejections (CME) both density and velocity can reach much larger values. Embedded into the solar wind is also the Interplanetary Magnetic Field(IMF). The solar wind behaves like an ideal plasma, where the magnetic field is "frozen in" to the moving plasma. Frozen in means that the plasma and magnetic field lines move in unison, with very low levels of diffusion even over great distances. Upon reaching the Earth, the IMF will connect to the magnetic field of the Earth, and a complex process of plasma transport and magnetic field line deformation will begin. This process is called the Dungey Cycle.

### 2.2.2 Magnetic re-connection

Originally suggested by J. W. Dungey in 1961, the Dungey cycle describes the process of how the IMF interacts with the Earth's magnetic field. When the solar wind carrying the IMF collides with the magnetic field of Earth if will be either parallel or anti-parallel in the north/south orientation to that of the Earth. If it is parallel the IMF will apply a pressure to the geomagnetic field before being deflected around the Earth. If it is anti-parallel however the magnetic field lines will break coherency, and instead the sun and Earth field lines will connect to one another. This will create long elongated magnetic field lines origination from the Earth and stretching into space and all the way back to the sun. The open field lines will still be anchored to the Earth. Since the solar wind plasma north and south of the Earth's magnetic field is still in motion and the frozen-in condition is not violated the field lines will still be moving outside the magnetos-pause. The solar wind motion will drag the field lines from the day-side and onto the night-side. This dragging of the field lines then give rise to a whole system of magnetic perturbations, electrical currents and additional re-connections on the night-side.

### 2.2.3 The details of the Dungey cycle

In Figure 2.2, the different magnetic field lines are numbered. Although each field line can look like this at some instant of time, it is better to think of it as the time evolution of the first line. It is also important to note that although it is convenient to think of this system as a step by step process, the entire cycle is running continually. For there to be a cycle an equal number of day-side and night-side re-connections must take place. As a result, for line 2 to move to position 3, the previous line 3 must have moved to position 4 etc. For this example, the focus will be kept on the evolution of a single line starting at position 1, but keep in mind that this is very much a moving system.

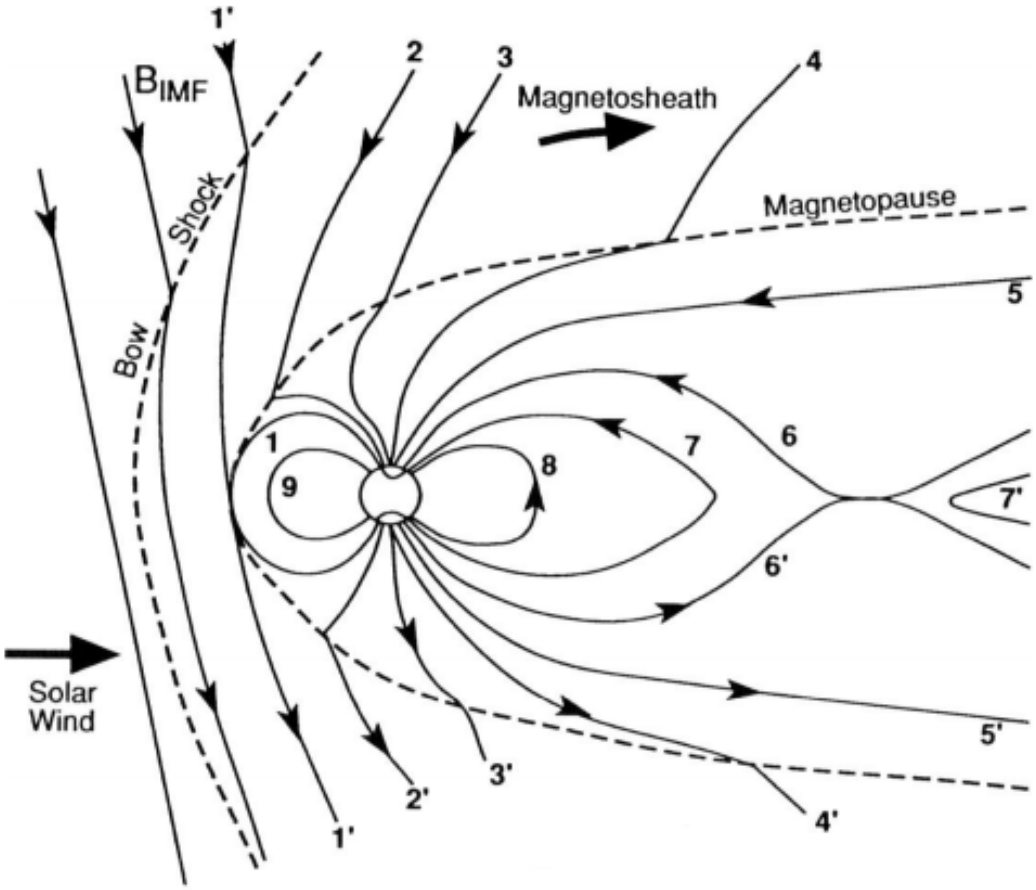


Figure 2.2: Illustration of the Dungey cycle

Initially, there is a very strong curl in the magnetic field in the immediate area where the magnetic re-connection has just happened. Following the induction equation (2.17b), a current $\mathbf{J}$ will arise pointing out of the figure plane. This will set up the $\mathbf{J} \times \mathbf{B}$ force described in the momentum equation (2.15) which will attempt to "smooth" the field line and straighten it out. This moves the field line from position 1 to position 2, and finally

to position 3. Here the field line have become straight, but the solar wind outside the magneto-pause is still moving away from the sun. Since the magnetic field is still frozen-in to the plasma, the field lines are now stretch toward the night-side. Since the plasma is moving with a magnetic field, the simplified ohm's law (2.16 for ideal plasma) gives rise to an electric field. The solar wind is moving to the right, and the magnetic field is pointing down, but at an angle. The resulting $\mathbf{E} \times \mathbf{B}$ Poynting vector is then pointing down and to the right, and push the magnetic field lines into the magnetopause. This is visible for line 4 in the Figure.

As the field line is dragged further back, a curl in the magnetic field will happen at the magnetopause, and give rise to another $\mathbf{J} \times \mathbf{B}$ force pushing toward the day-side. This force will decelerate the plasma entering the magnetopause, and straighten the field lines as they are pushed downwards. When looking at line 5, the plasma is now inside the magnetosphere and is moving downwards. The magnetic field is pointing to the left and the Electric field will still point out of the plane, and the Poynting vector will continue to push the magnetic field line towards the equatorial plane.

As the magnetic field lines are pushed closer and closer together, they form a thin plasma sheet with a strong current. In this narrow region, the magnetic field lines are anti-parallel and the night-side re-connection occurs to become closed field lines. This is what happens at line 6 on the figure. Since the newly reconnected field line has a strong magnetic curl it gives rise to another Lorentz force. This time the magnetic field line is pushed inwards to the Earth. As more and more field lines are re-connected and pushed inwards, the magnetic pressure builds, and the field lines will drift back towards the day-side (line 7, 8 and 9). This completes the Dungey Cycle, and describes how magnetic field lines are transported from the day-side to the night-side, and then back to the day-side again.

### 2.2.4 Ionospheric currents

The previous section dealt with how the magnetic field at large behaves during the opening and closing of magnetic field lines. This section shows the part the ionosphere plays in this cycle, and how the Dungey cycle gives rise to currents, electric fields and magnetic perturbations.

When the solar wind drags the field lines towards the night-side, they are not moved immediately in the ionosphere. In the ionosphere there is a much greater particle density than in the magnetosphere, and the plasma will become collisional. Looking back at equation (2.15), there is a term $\mathbf{P}$. This collisional pressure term will resist the attempted

motion of the magnetic field line and anchor them in place. Because the field line is still moving outside the ionosphere, there will be a kink in the field line. Although the term in the equation is called the pressure term, physically it is caused by the collision of plasma as it attempts to move through the ionosphere, together with the magnetic field lines.

As can be seen in Figure 2.3, this kink will now add a curl to the magnetic field line. Following Ampére's law (2.17a), this will set up a current. It is important to note that while Ampére's law does describe the origin of such a current, this is not an isolated phenomena. Simultaneously there will be currents flowing along the field lines up to the magnetopause where the same event transpires in the opposite direction, thereby closing the loop. The current in the ionosphere now creates a $\mathbf{J} \times \mathbf{B}$ Lorentz force. As the kink becomes greater, the current will be stronger. When the current becomes sufficiently strong, the force will be greater than that of the collision pressure friction, and the magnetic field line will be accelerated. The same process repeats when the magnetic field lines are moving back towards the day-side. Although the presence of neutral particles breaks the ideal plasma conditions this phenomenon still occurs, albeit with some diffusion of the magnetic field lines. There is now a current along the magnetopause, and a current along the ionosphere. The FAC are then generated by the need for convection matching. The kink in the magnetic field just above the ionosphere is, if viewed from above, a perturbation in the magnetic field. Because only the open field lines are bent, there will be a perturbation relative to the unperturbed neighbours. This local perturbation causes a curl, which is where the current flows along the magnetic field lines.

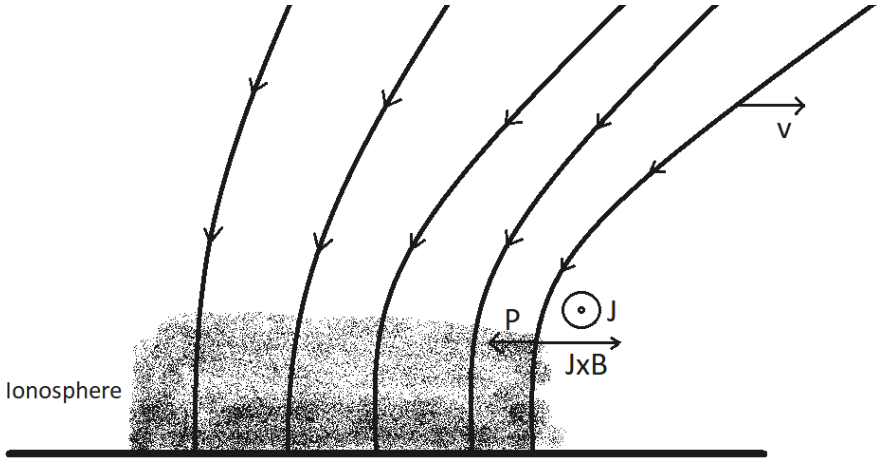


Figure 2.3: Simplified 2 dimensional drawing of how the pressure stops the magnetic field line from moving, and how the increasing JxB term eventually overcomes it

Figure 2.4 show the collected system of how all these currents acts combined. The Pederson

currents is set up by the kinks in magnetic field lines and the field aligned currents by the perturbed field lines.

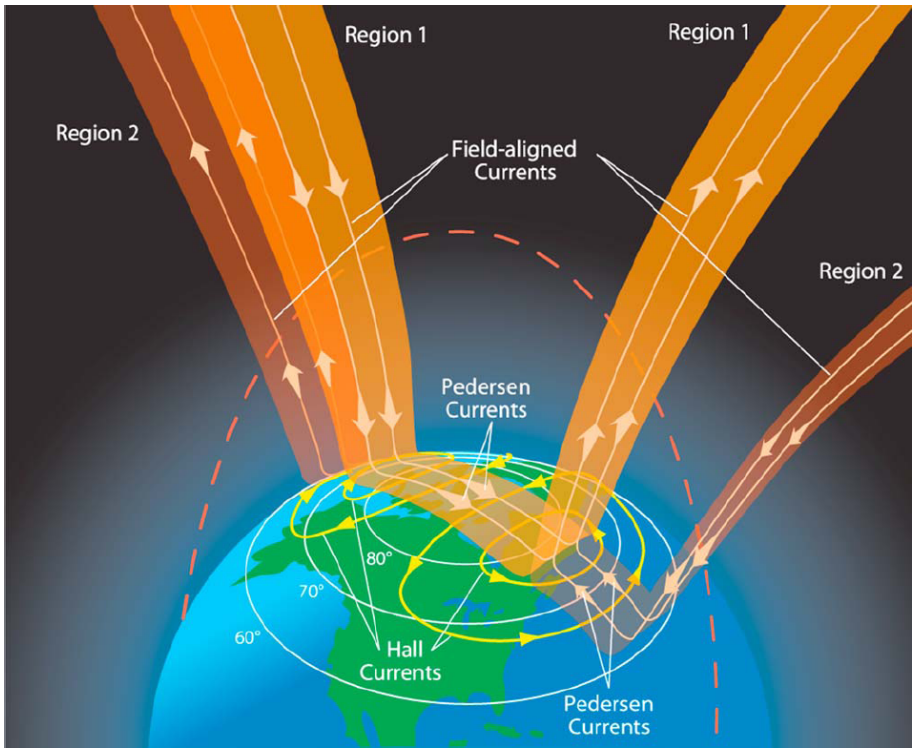


Figure 2.4: Figure from American Geophysical Union, Washington, DC, USA, showing the complete system of currents above the Earth [19]

## 2.3 Conductivity in the ionosphere

### 2.3.1 Plasma conductivity in the presence of neutral particles

In section 2.1.3 we introduced the plasma resistivity $\eta$. For the solar wind and most of the plasma within the Earth's magnetosphere this was set to 0, since this plasma is collision-less. With the plasma conductivity being the inverse of resistivity, one could say that conductivity is infinite in space plasma. In the ionosphere however, there are neutral particles that cause collisions and conductivity cannot simply be set to infinity.

Returning to equation (2.4), the equation of motion for a charged particle. This equation assumes that the particle will be exclusively governed by the electric and magnetic fields present, and any near collision with another charged particle can be described through changes in these microscopic fields. In the neutral atmosphere there will be an additional

term, which is the momentum change due to collisions with neutral atoms.

$$m\frac{\partial \mathbf{v}}{\partial t} = q(\mathbf{E} + \mathbf{v} \times \mathbf{B}) - m\nu_c(\mathbf{v} - \mathbf{u}) \tag{2.20}$$

$\mathbf{u}$ is here the velocity of the neutral collision partner, and $\nu_c$ is the collision frequency. This term is sometimes called the friction term, since it impedes motion. Neglecting the magnetic field, assuming a steady state and collision partners at rest, the electric field can be described as:

$$\mathbf{E} = -\frac{m_e\nu_c}{e}\mathbf{v}_e \tag{2.21}$$

Since the electrons are moving with respect to the ions, they carry the current $\mathbf{J} = -en_e\mathbf{v}_e$. Substituting into equation (2.21) yields.

$$\mathbf{E} = \frac{m_e\nu_c}{n_e e^2}\mathbf{J} \tag{2.22}$$

This is familiar to Ohm's law, which states that $J = \sigma_0 E$, where $\sigma_0 = \eta^-1$ and $\eta$ and $\sigma_0$ are defined as.

$$\eta = \frac{m_e\nu_c}{n_e e^2} \tag{2.23a}$$

$$\sigma_0 = \frac{n_e e^2}{m_e\nu_c} \tag{2.23b}$$

In the lower parts of the ionosphere the magnetic field will have a strong influence, and must therefore be included. Starting from equation (2.20) with the magnetic field present, a steady state and collision partners at rest yields:

$$\mathbf{E} + \mathbf{v}_e \times \mathbf{B} = -\frac{m_e\nu_c}{e}\mathbf{v}_e \tag{2.24}$$

If substituting for the definition for $\sigma_0$ from equation (2.23b) and applying the current density definition $\mathbf{J} = -en_e\mathbf{v}_e$, equation (2.24) becomes:

$$\mathbf{J} = \sigma_0\mathbf{E} - \frac{\sigma_0}{n_e e}\mathbf{J} \times \mathbf{B} \tag{2.25}$$

One can then assume that the magnetic field is aligned with the z axis, so that $\mathbf{B} = B\hat{\mathbf{e}}_z$. Any charged particle in motion will do some gyration around some line where the gyro-frequency is given as:

$$\omega_g = \frac{qB}{m} \tag{2.26}$$

Inserting equation (2.26) into (2.25) and solving for each component of $\mathbf{J}$, they can be found as:

$$J_x = \sigma_0 E_x + \frac{\omega_{ge}}{\nu_c} J_y \tag{2.27a}$$

$$J_y = \sigma_0 E_y - \frac{\omega_{ge}}{\nu_c} J_x \tag{2.27b}$$

$$J_z = \sigma_0 E_z \tag{2.27c}$$

Combining (2.27a) and (2.27b) to first eliminate $J_y$ from (2.27a) and then eliminate $J_x$ from (2.27b) gives the final result:

$$J_x = \frac{\nu_c^2}{\nu_c^2 + \omega_{ge}^2} \sigma_0 E_x + \frac{\omega_{ge}\nu_c}{\nu_c^2 + \omega_{ge}^2} \sigma_0 E_y \tag{2.28a}$$

$$J_y = \frac{\nu_c^2}{\nu_c^2 + \omega_{ge}^2} \sigma_0 E_y - \frac{\omega_{ge}\nu_c}{\nu_c^2 + \omega_{ge}^2} \sigma_0 E_x \tag{2.28b}$$

$$J_z = \sigma_0 E_z \tag{2.28c}$$

This set of components can be written in dyadic notation $\mathbf{J} = \sigma \mathbf{E}$. Each tensor will then read:

$$\sigma = \begin{pmatrix} \sigma_P & -\sigma_H & 0 \\ \sigma_H & \sigma_P & 0 \\ 0 & 0 & \sigma_{||} \end{pmatrix} \tag{2.29}$$

Where the tensor elements are defined as.

$$\sigma_P = \frac{\nu_c^2}{\nu_c^2 + \omega_{ge}^2} \sigma_0 \tag{2.30a}$$

$$\sigma_H = \frac{\omega_{ge}\nu_c}{\nu_c^2 + \omega_{ge}^2} \sigma_0 \tag{2.30b}$$

$$\sigma_{||} = \sigma_0 = \frac{n_e e^2}{m_e \nu_c} \tag{2.30c}$$

These tensor elements are the Hall Conductivity $\sigma_H$ and the Pedersen conductivity $\sigma_P$. The Pedersen conductivity governs the currents along the electric field that is transverse to the magnetic field. The Hall conductivity determines the current that is perpendicular to both the magnetic field and the electric field, in the $-\mathbf{E} \times \mathbf{B}$ direction. $\sigma_{||}$ is the parallel conductivity and governs any current parallel to the magnetic field.

### 2.3.2 The solar contribution

One of the main contributors to ionization on the day-side is the sun. Ultraviolet radiation from the sun will ionize neutral atoms and increase the electron density during the day.

After sunset the ions and electrons recombine and resets the balance [20]. Since the plasma conductivity $\sigma_0$ has an electron density $n_e$ dependency, the Hall and Pedersen conductivity will increase when the sun is above the horizon. Figure 2.5 show an example of how a typical ionosphere profile for day and night looks.

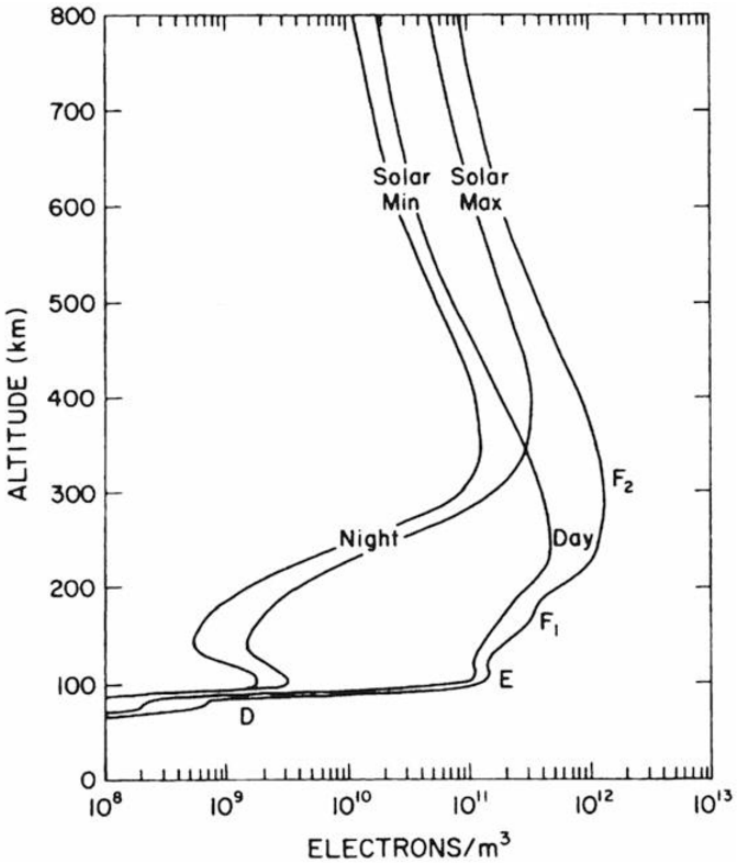


Figure 2.5: Typical electron density profile for day and night. Notice that the greatest difference is in the D and E regions between 100km and 200km. This is the area which will be surveyed later [21]

## 2.4 Conductivity and ionospheric currents

If the FACs transport electrons and ions into and out of the ionosphere and since the plasma conductivity is dependent on electron density, temperature and collision frequency, a relationship between the two might be assumed. The Knight relation (Knight, 1972) established a mathematical relation between upward field-aligned current and the energy of downward precipitation electrons. The relationship between precipitating particles and the local height integrated conductivity was empirically shown later (e.g. Robinson et al., Lumerzheim et al., 1991). The relationship between field aligned currents was then

proposed (Ridley et al,. 2002) and empirically shown (Robinson et al., 2019). This relationship is what this thesis will investigate.

# Chapter 3

# Data observation

In this chapter the experiments used in this study are introduced. The Svalbard European Incoherent SCATter(EISCAT) radar provided the Hall and Pedersen conductivities in the lower ionosphere. The Active Magnetosphere and Planetary Electrodynamics Response Experiment(AMPERE) database was accessed to provide the upper ionospheric FACs, and a complete review of the total amount of data and the yearly spread of these is be given.

## 3.1 The EISCAT Svalbard radar

In the use of this thesis the period of 2010-2017 was selected for use. Throughout this period the EISCAT radar is not running constantly. For that reason the up-time dates are scattered throughout the years. For each experiment, the radar is not always running full days either, and sometimes multiple experiments are run in interval during the same day. For the data acquired, we chose the IPY(International Polar Year) experiments since they provided sufficient accuracy for the relevant height-profile and a high quantity of experiments. A duration of at least 6 hours for each experiments was also demanded before being used.

### 3.1.1 The unprocessed EISCAT readings

EISCAT Svalbard is an incoherent scatter radar located on the Island of Spitsbergen on Svalbard Norway. It consists of two separate radar dishes, one movable and one fixed pointing along the magnetic field line. For this thesis measurements derived from the fixed radar-dish are used. The EISCAT radar fires a series of short radio bursts into the sky and measures the radio signal from the electron resonance that is scattered back.

From this resonance the electron density and temperature is estimated for different layers of height in the atmosphere. The height resolution is roughly 4 kilometers between each separate data point depending on the mode used, and varies slightly between measurements. The radar can measure electrons up to an altitude of 500km. As the radar collects measurements, these measurements are sampled and some average is then derived. The time between each sampling varies depending on the experiment, but often it is as low as one minute and rarely any longer than 10 minutes. This gives an excellent resolution that is on par with the readings collected from the AMPERE array. All the data gathered from these experiments are then stored in the Madrigal database for public use [22]

From these radar readings and the NRLMSISE-00 model, height profiles of the Pedersen conductivity and the Hall conductivity are derived. These are collected from the Madrigal database. Based on the radar readings the conductivity is calculated using equations (2.30a) and (2.30b), with (2.30c) being the basis for $\sigma_0$. The collision frequency is estimated based on the electron temperature and the amount of neutral collision partners, and are also stored in the Madrigal database.

What is most often used to estimate the total activity in the lower ionosphere, are the height integrated conductivities between heights of 80 and 200 kilometers. Above these altitudes the neutral-ion collision frequency is so small that the conductivity becomes negligible. Below 80 kilometers altitude there are hardly any ions, since most of the ionizing sunlight have already been absorbed by the higher atmosphere, and space plasma does not exist below such altitudes. In the event of ionization, the recombination rate at this lower altitude will neutralize it rapidly. Plasma conductivity is therefore negligible in this region.

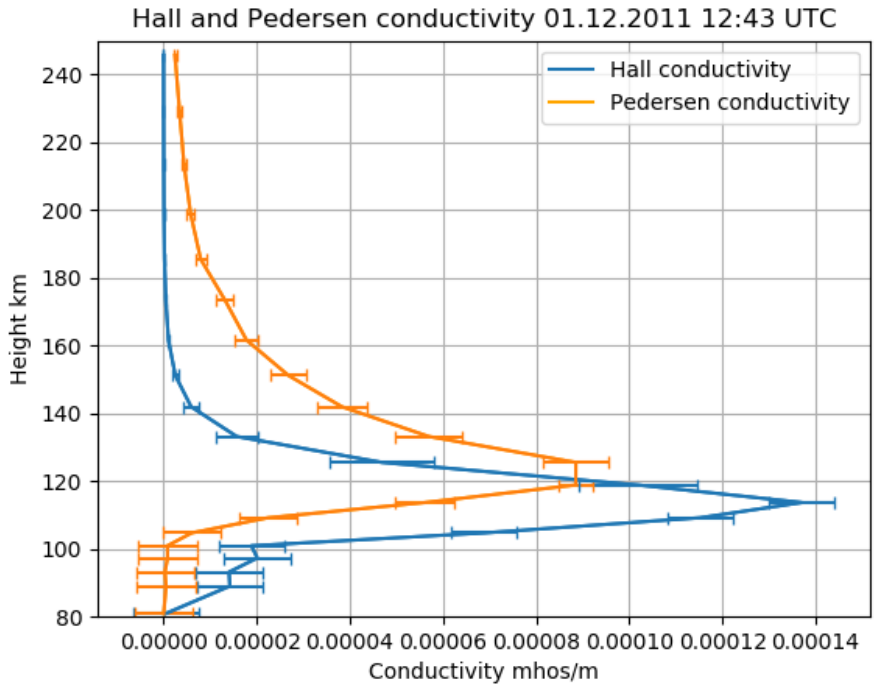


Figure 3.1: Conductivity derived by madrigal for each height layer between 80km and 250km, as measured by the EISCAT radar.

Figure 3.1 shows the height-dependent conductivity. As previously stated we are interested in getting the time-dependent conductance. This is found by integrating the area of the height-dependent conductivity over the total height.

$$\Sigma_H = \int_{80}^{200} \sigma_H dh \tag{3.1a}$$

$$\Sigma_P = \int_{80}^{200} \sigma_P dh \tag{3.1b}$$

Equation (3.1a) and (3.1b) will provide the conductance for each time the height profiles are derived from the radar. The variance in conductivity in each height-layer does not correspond to any simple equation, and it is therefore difficult to approximate some curve that would fit the data. Instead we chose to draw the conductivity as a multi sided object and measure the area inside. Figure 3.2 shows an example of the time dependent conductance. To finalize the data we compress it so each point of data is the average of a 10 minute interval. This allows simpler methods of comparison. Figure 3.3 shows an example of this.

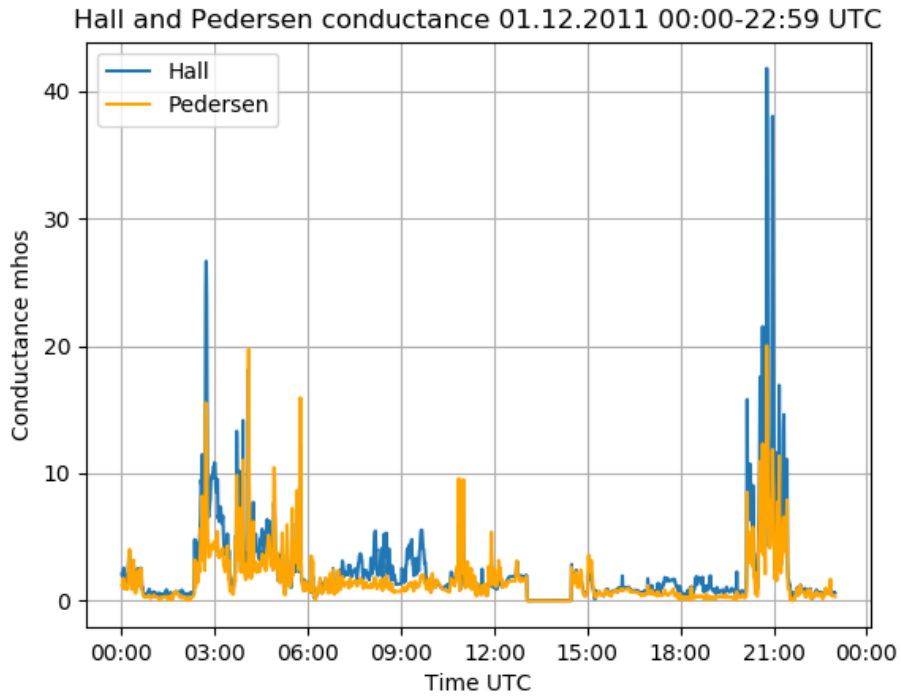


Figure 3.2: Height integrated conductance obtained from integration of Madrigal profiles as a function of time.

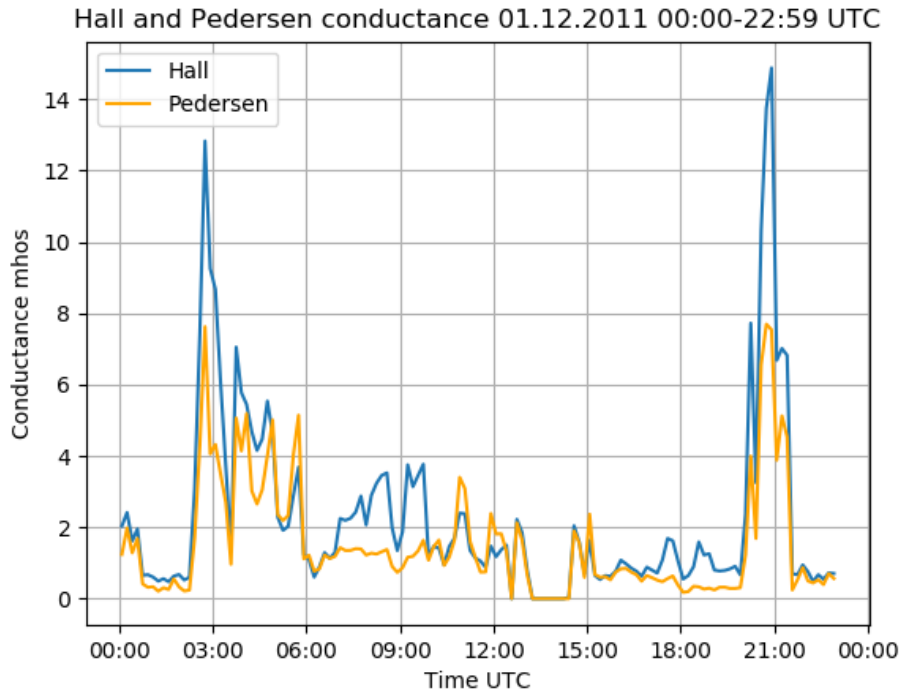


Figure 3.3: Hall and Pedersen conductance averaged over 10 minute intervals.

### 3.1.2 Errors in the measured data

There are of course uncertainties in the data provided by Madrigal. In Figure 3.1 the horizontal error-bars show these uncertainties as provided by Madrigal. Since we will be using large sets of data we assume that the uncertainties of each individual data point becomes less relevant. There are still some sources of errors that must be ruled out. The main source of errors in the EISCAT data are spikes. Although one can assume that most data will be good and that some exaggerations or minor errors will be smoothed out when averaged over 10 minutes, spikes will result in bad data. Figure 3.4 shows a spike of several hundred times the previous values. This is physically impossible, and it must therefore be removed.

A way of getting rid of data spikes is to ignore such outlying values in the data-set. For this thesis a maximum accepted value of 60 mhos was selected for the exclusion. This does create some uncertainty as there might be times of sustained activity that produce values higher than this anticipated maximum. After manual inspection of the entire data-set used this was found not to be the case in any of the selected experiments.

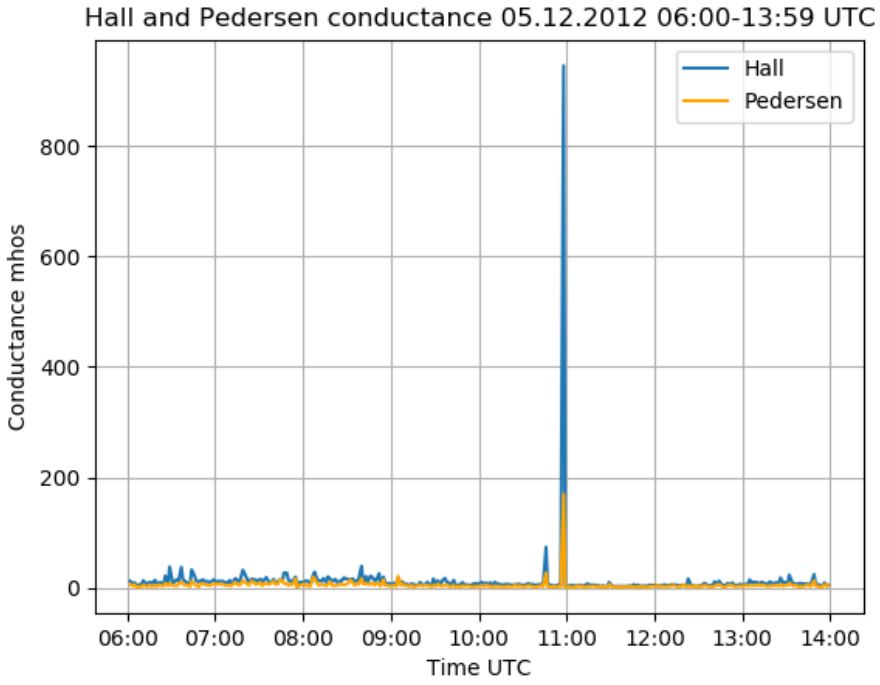


Figure 3.4: Data spike showing in an unadjusted file from Madrigal.

Additionally there are errors that are not registered as spikes in the conductance itself. Spikes in the conductivity can result in false conductance readings that is within the expected levels. An example of this is shown in Figure 3.5. Here the conductivity is

spiking for every other data-point, resulting in conductances that are within the activity levels we expect, yet the data is very likely wrong. This date and other with similar errors are subsequently removed from the data-set used.

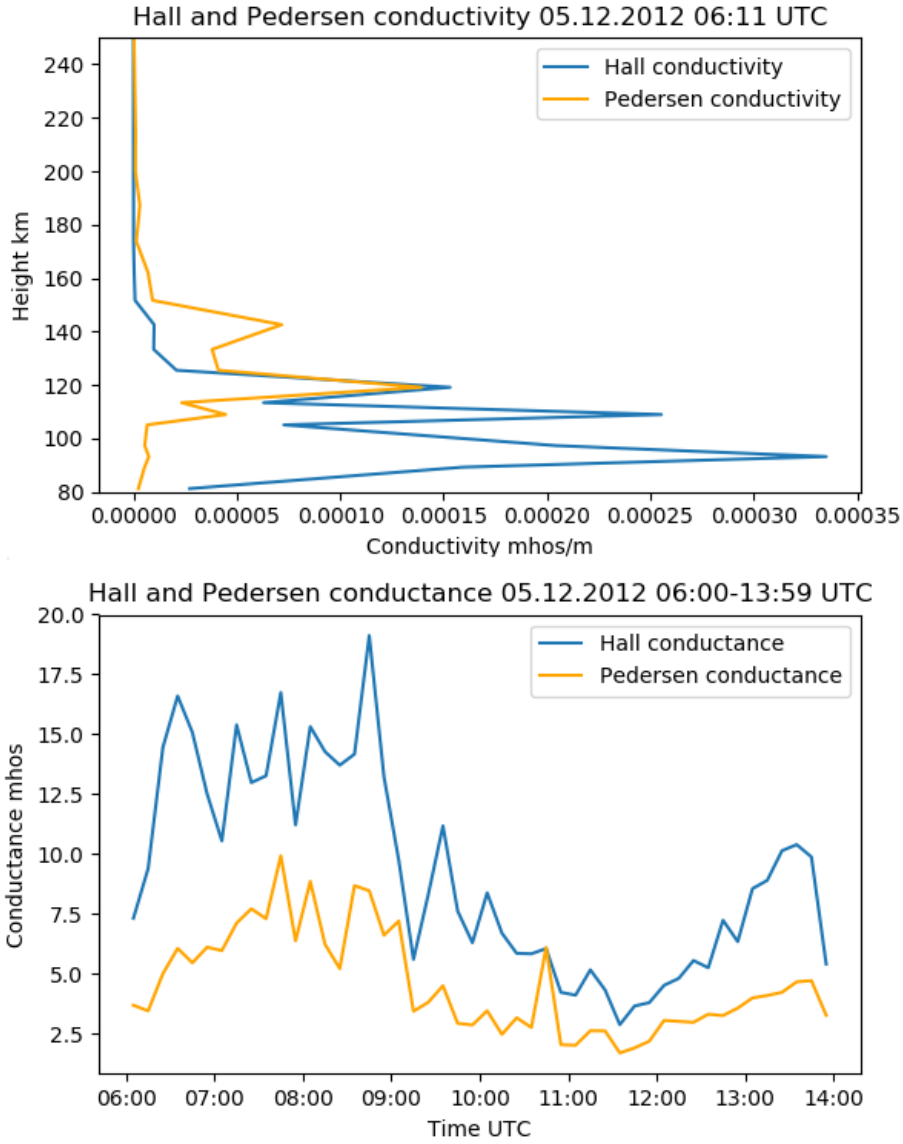


Figure 3.5: Spikes in conductivity resulting in conductances within the expected levels that nonetheless are incorrect.

### 3.1.3 Removing the Solar contribution

As mentioned in section 2.3.2, the sun affects the ion and electron density in the ionosphere, and these will consequently affect the Hall and Pedersen conductance. To accurately study any relationship between conductance and FACs, the solar contribution must be removed. One way to see the contribution from the sun is to look at all the data as a function

of solar zenith angle. The smooth increase in minimum conductance as the solar zenith angle decreases can be assumed to the the solar contribution. This can be seen in Figure 3.6

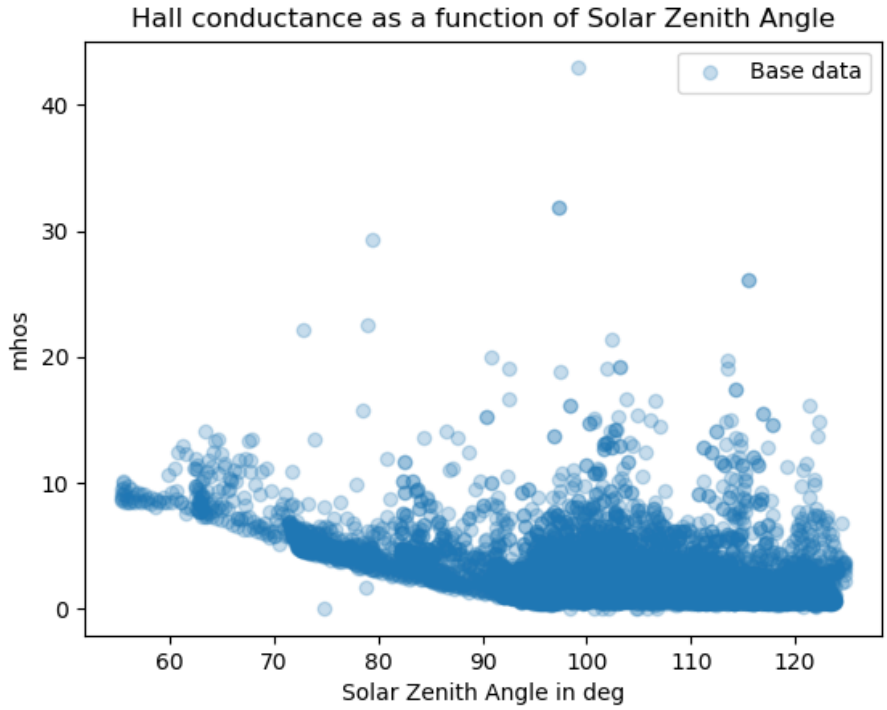


Figure 3.6: Hall conductance. With the exception of 2 points, the minimum conductance increase noticeably when $\chi$ becomes smaller than 90 degrees.

Multiple studies have been conducted in an attempt to model this dependency empirically. Brekke and Moen (1993)[23] made adjustments to previous studies and found that the solar flux and solar zenith angle dependence of Hall and Pedersen conductances could be well represented by:

$$\Sigma_H = S_\alpha^{0.53}(0.81cos\chi + 0.54cos^{0.5}\chi) \tag{3.2a}$$

$$\Sigma_P = S_\alpha^{0.49}(0.34cos\chi + 0.93cos^{0.5}\chi) \tag{3.2b}$$

Where $S_\alpha$ is the 10.7cm solar flux, and $\chi$ is the solar zenith angle. Lilensten et al., (1996)[24] found that the solar contribution could be found with the following equation:

$$\Sigma_{H,P} = (a_1 f_{10.7} + a_2)cos(\chi) + (b_1 f_{10.7} + b_2)cos(\chi)^{0.5} + (c_1 f_{10.7} + c_2) \tag{3.3}$$

Where the coefficients a, b and c were fitted empirically. There has also been multiple later studies as-well, some attempting to neglect the solar flux and have only a solar zenith dependency. (Ieda et al, 2014)[25] Applying these different methods we now show

the results of the EISCAT Svalbard data.

Figure 3.7 shows the Brekke and Moen fit for the Hall conductance for the time covered by our data set. The proposed solar contribution does not match the minimum line of the derived data. The Brekke and Moen equation produces multiple green lines. This is because the data is taken from multiple different years, resulting in different $f_{10.7}$ values. The fit for Pedersen conductance was about the same. Figure 3.7 also shows that the solar contribution predicted by Brekke and Moen is larger than the conductance derived from the EISCAT Svalbard radar in some places. This could be because Brekke and Moen used the Tromsø EISCAT radar, and typical ionospheric conditions at Svalbard are different.

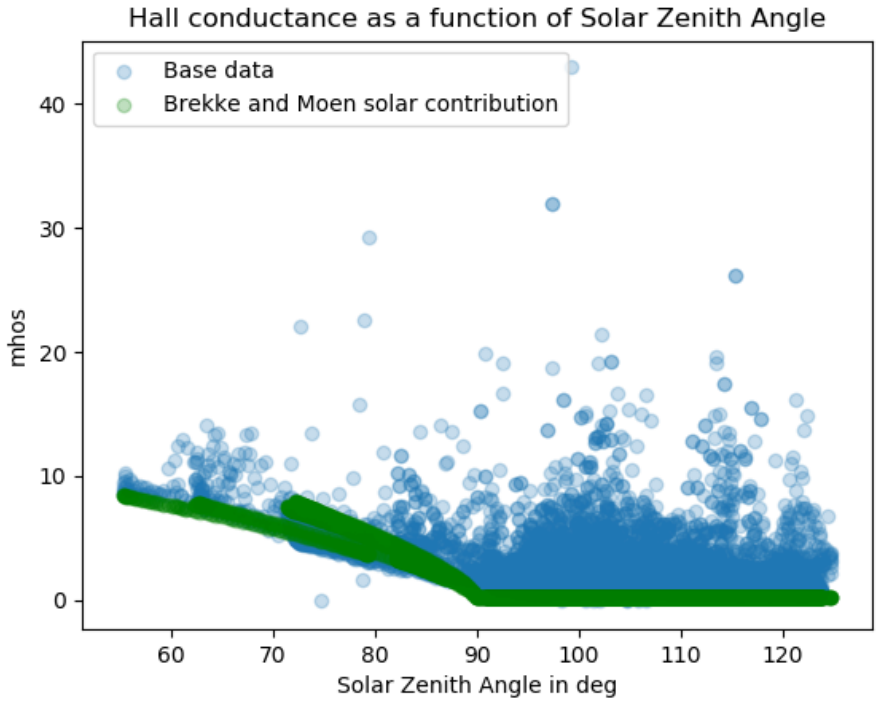


Figure 3.7: Hall conductance in blue, and the Brekke and Moen solar contribution in green.

Next, Figure 3.8 shows the same comparison for the Lilensten equations for the Pedersen conductance. Using the coefficients provided in Lilensten's paper, the Hall conductance had a better fit than the Brekke and Moen equations. The Pedersen conductance fit was however inaccurate. The Lilensten solar contribution also creates several smooth lines, since several different years are used, each with a different $f_{10.7}$ value.

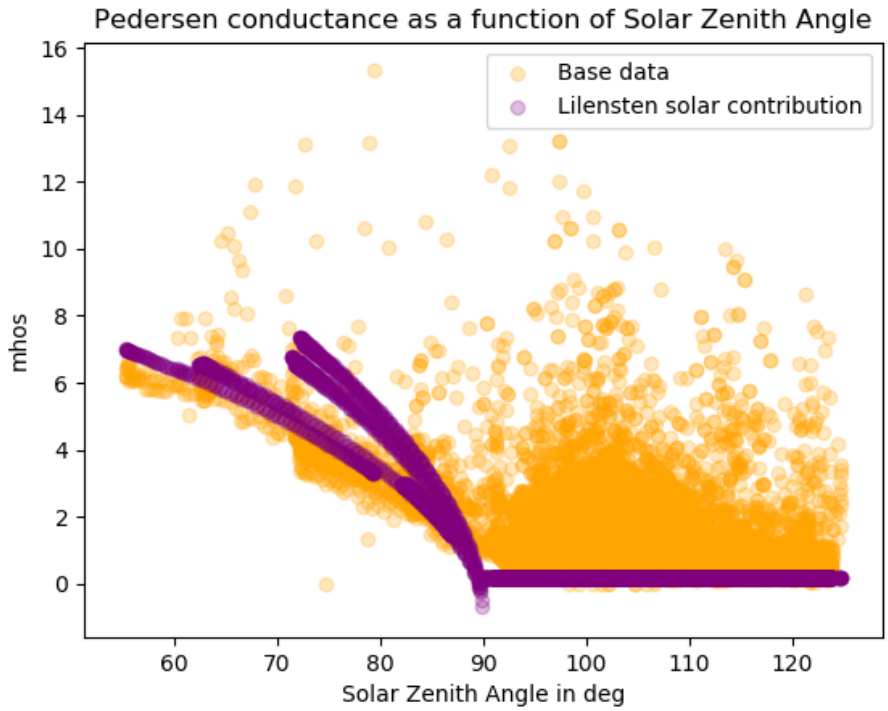


Figure 3.8: Pedersen conductance in orange, and the Lilensten solar contribution in purple.

Using Ieda's method also provided no accurate estimates for the solar contribution. All the above methods do admit that the coefficients will likely have to be adjusted to use with different sets of data. For the purpose of this thesis however, it is not necessary to perfect the method of accurately modeling the solar contribution. In Figure 3.6, all we are need is for the minimum values when the sun is above the horizon to match the minimum values of the rest of the data. This will result in some loss of accuracy, but summer and spring measurements are a small percentage of our total data. This result for the Hall conductance is shown in Figure 3.9. The result for Pedersen conductance was similar.

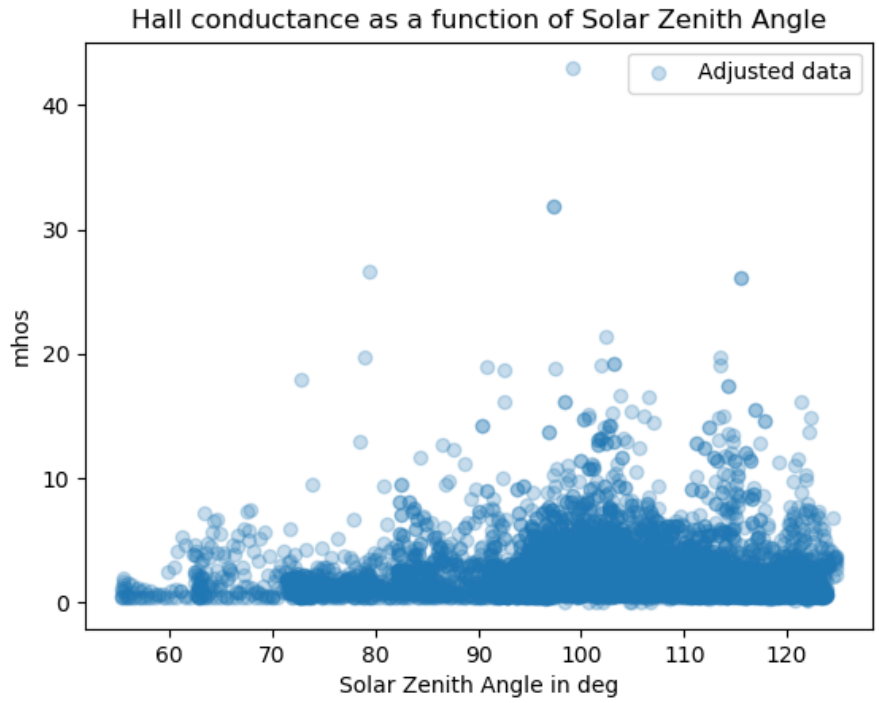


Figure 3.9: Adjusted Hall conductance based on minimum value bin subtraction. This crude method provided better results than the line fits.

## 3.2 The AMPERE experiment

### 3.2.1 The unprocessed AMPERE data

To find the FACs in the polar cap region AMPERE is used. This is an experiment that collects data from the Iridium communications satellites. This constellation of satellites orbit the Earth in an altitude of 780 kilometers in near circular polar orbits. The fleet of 66 satellites gives a decent continual coverage as there will be multiple satellites within the polar cap region at any given time. Although the presence of multiple satellites does provide good coverage, it does not provide homogeneous coverage of the entire polar cap. To fill in the blanks data is therefore interpolated between each satellite.

Each satellite is equipped with a magnetometer. When measured against the expected background magnetic field, the magnetic perturbations can be derived [16]. As explained in section 2.2.4, it is then possible to calculate the FACs. AMPERE provides the FAC measured in micro ampere per square meter $\mu A/m^2$ and its direction (up/down) for each grid point for a 24 hour period. Every 2 minutes a result is derived from the satellite measurements. The constellation follows a few discrete orbits with a 10 minute travel

time distance between each satellite. As a consequence the entire orbital path of each discrete orbit is mapped every 10 minutes.

The derived magnetometer measurements are provided on a grid in Altitude Adjusted Corrected Geomagnetic coordinates. This grid is organized into 24 longitudes spaced 15 degrees apart each representing an hour in Magnetic Local Time (MLT), with 50 points of latitude running north-south with one degree separation. This gives us far better resolution near the poles as the MLT longitudes are far closer in geographic separation here than they are further south. This grid is centered with respect to the position of the geomagnetic pole. As a consequence the Earth will rotate beneath a static grid. In Figure 3.10 the magnetic perturbations for each grid point are seen on the left side, with the appropriate FAC on the right side.

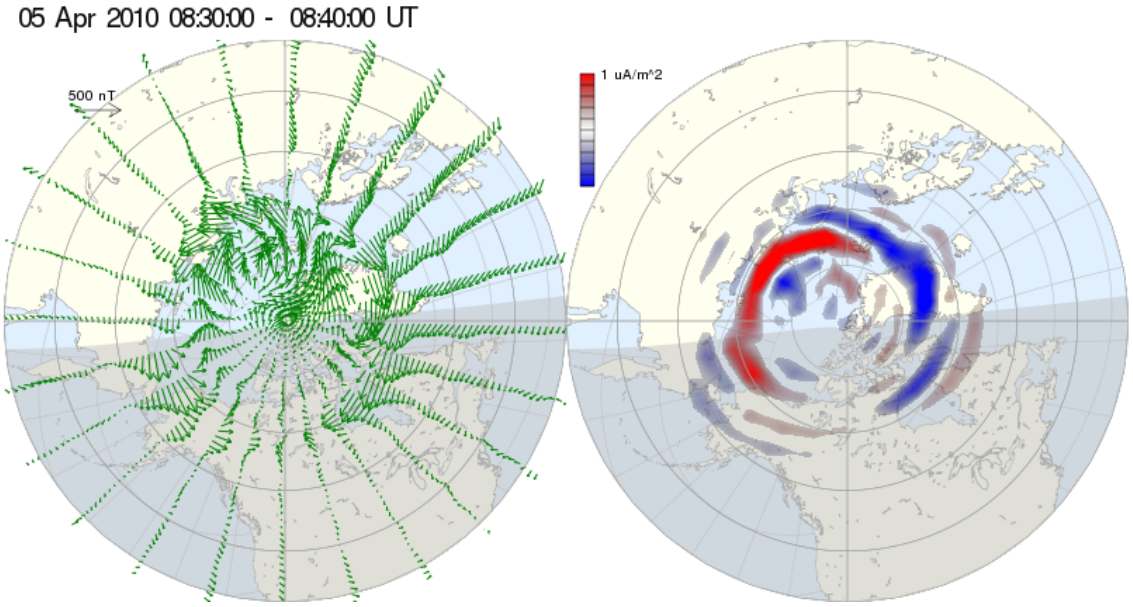


Figure 3.10: Example AMPERE data for April 5. 2010 at 08:30 UTC. The perturbations are fitted magnetometer variation vectors after spiraling harmonic fitting to raw satellite data.

For this study we have used the official ncdf files provided by the AMPERE database are used [17]. In the ncdf format each value is stored in a 720x1200 matrix. Each of the 1200 points provide the time-dependent FAC for a single coordinate. This gives a picture of the field-aligned current for the entire northern hemisphere at a 2 minute resolution. For this research only the immediate surroundings of the EISCAT Svalbard radar are needed. A method of selecting and estimating the FAC at the relevant location is therefore applied.

### 3.2.2 Spacial alignment of measurements

The EISCAT Svalbard radar beam cone has a width of 1.5 kilometers at 100 kilometers altitude. In contrast the AMPERE grid is spaced 109 kilometers latitudinal and 200 kilometers longitudinal in the vicinity of the radar coordinates. Exact conjunctions between Iridium satellites and the radar measured points are therefore unlikely to occur. To match up the radar measurements with the AMPERE grid we use the 4 closest grid points and weight them accordingly.

The magnetic invariant latitude of EISCAT is fixed at 75.18°for the entire rotational period of the Earth. The MLT for the radar can also be calculated from EISCAT's position since the time and geographic coordinates are known. Using these two provides an accurate geomagnetic position for every radar measurement. For each point we then identify and weight points from the AMPERE grid appropriately. Figure 3.11 shows an illustration of the radar position between four fictional AMPERE grid point.

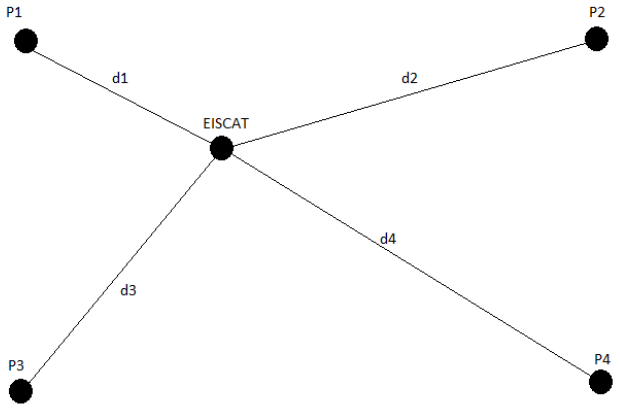


Figure 3.11: Illustration of distances from EISCAT to four AMPERE grid points.

To weight the points the appropriate length from the radar position to each AMPERE grid-point is required. Since the position of each grid point and the radar in terms of magnetic latitudes and longitudes are known, the haversine formula can be used to calculate the distances in a spherical geometry.

$$A = \sin^2\left(\frac{\Delta\psi}{2}\right) + \cos(\psi_1)\cos(\psi_2)\sin\left(\frac{\Delta\lambda}{2}\right) \tag{3.3a}$$

$$D = 2r\arctan\left(\frac{\sqrt{A}}{\sqrt{1-A}}\right) \tag{3.3b}$$

Here, D is the distance between two points, r is the radius of Earth plus the measurement height, $\psi_1$ and $\psi_2$ are the latitudes of the two points being compared, with $\Delta\psi$ being

the latitudinal difference and $\Delta\lambda$ being the longitudinal difference. Here, we assume that the invariant latitude and MLT coordinates are a proper spherical coordinate system. In reality this is not the case, but the method is deemed sufficient since we are using coordinates in close proximity with one another. Using this method each point can be attributed the appropriate weight based on their distance to the radar using the standard weight for multiple distances.

$$\omega_1 = \frac{d_2 d_3 d_4}{d_1 d_2 d_3 + d_1 d_2 d_4 + d_1 d_3 d_4 + d_2 d_3 d_4} \tag{3.4a}$$

$$\omega_2 = \frac{d_1 d_3 d_4}{d_1 d_2 d_3 + d_1 d_2 d_4 + d_1 d_3 d_4 + d_2 d_3 d_4} \tag{3.4b}$$

$$\omega_3 = \frac{d_1 d_2 d_4}{d_1 d_2 d_3 + d_1 d_2 d_4 + d_1 d_3 d_4 + d_2 d_3 d_4} \tag{3.4c}$$

$$\omega_4 = \frac{d_1 d_2 d_3}{d_1 d_2 d_3 + d_1 d_2 d_4 + d_1 d_3 d_4 + d_2 d_3 d_4} \tag{3.4d}$$

Multiplying each weight with their respective AMPERE point and adding them yields the results for the approximation of the FAC value at each radar position. Having done this for each point in time, the varying currents above the radar position can then be obtained for a full day. Figure 3.12 shows an example of this.

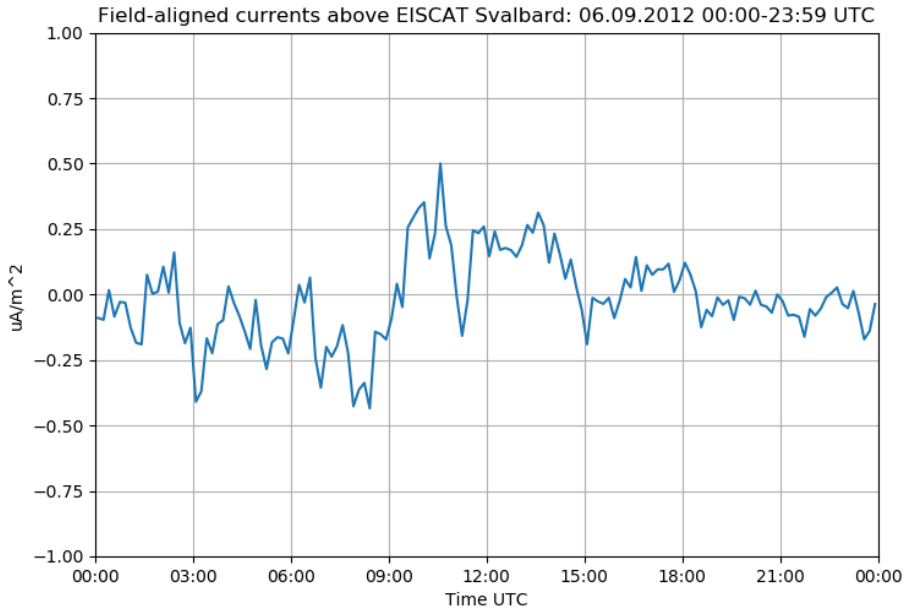


Figure 3.12: Variation of the FACs of the higher ionosphere as they would be measured above the EISCAT radar. This plot follows the radar as it rotates beneath the AMPERE data-grid.

In using the AMPERE data one must assume that the interpolation done is sufficiently

accurate to use without consideration of where the satellites are actually taking measurements in real time. One must also assume that the current strength is behaving roughly linearly between each grid point, and that any local peaks or dips between are insignificant. Discussions on these limitations in the AMPERE data can be found here[26][27].

Having extracted the necessary data a comparison between the Hall and Pedersen conductance provided by EISCAT, and FAC provided by AMPERE can be done. To make the comparisons accurate both experiments must be integrated over the same intervals of time. Since the cadence of the AMPERE experiment is 10 minutes, this is chosen as the standard time interval. The timing chosen for both experiments is so that each point of data encompasses the periods 00:00-00:10 UTC, 00:10-00:20 UTC and so forth.

## 3.3 Review of the selected data

In this section a brief overview of the total amount of data selected is provided.

Like the EISCAT radar, the AMPERE database does not have 100% up-time. As such, some EISCAT experiments had to be discarded. When all the EISCAT experiments with satisfying lengths and proper AMPERE up-time was accounted for, a total of 80 experiments over an equal number of days were collected. The total amount of unique data points is 7670 which corresponds to 1286,2 Radar hours.

| Month/Year | 2010 | 2011 | 2012 | 2013 | 2014 | 2015 | 2016 | 2017 | Total |
|---|---|---|---|---|---|---|---|---|---|
| January | 129.5 | | 174.8 | 85.0 | 79.3 | | | 165.3 | 633.9 |
| February | | | | | | | 175.5 | 34.0 | 209.5 |
| Mars | | | | | | | | | |
| April | | | | | 61.7 | | | | 61.7 |
| May | | | | | | | | | |
| June | | | | | | | | | |
| July | 24.5 | | | | | | | | 24.5 |
| August | 30.7 | | | | | | | | 30.7 |
| September | | | 62.2 | | | | | | 62.2 |
| October | | | | | | | 85.3 | | 85.3 |
| November | 39.0 | 44.0 | | | | 7.0 | | | 90.0 |
| December | | 28.2 | | | | | 52.3 | | 80.5 |
| Total | 223.7 | 72.2 | 237.0 | 85.0 | 141.0 | 7.0 | 313.1 | 199.3 | 1286.2 |

Table 3.1: Total hours of experiments for each month and year for the 2010-2017 period.

Table 3.1 shows the distribution of experiments for each month and year. There is much better coverage during the winter than during the summer. This leaves a total of 1021.8

hours of experiments where the sun is either completely absent versus only 264.4 hours where it is partially present. Any inaccuracies resulting from the method applied to remove the solar contribution will therefore be of less significance.

Since the radar usually does not operate for full days at a time there is some distribution for time of day as well. This distribution is shown in Figure 3.13. There is better coverage during midday and afternoon than during the early morning. This is due to some experiments not starting before 08:00 UTC. In Chapter 4 it will be shown how both the average current and conductivity varies by time of day. Going forward we will replace UTC with MLT. This is done since MLT is far more relevant to the expected variances than what UTC is.

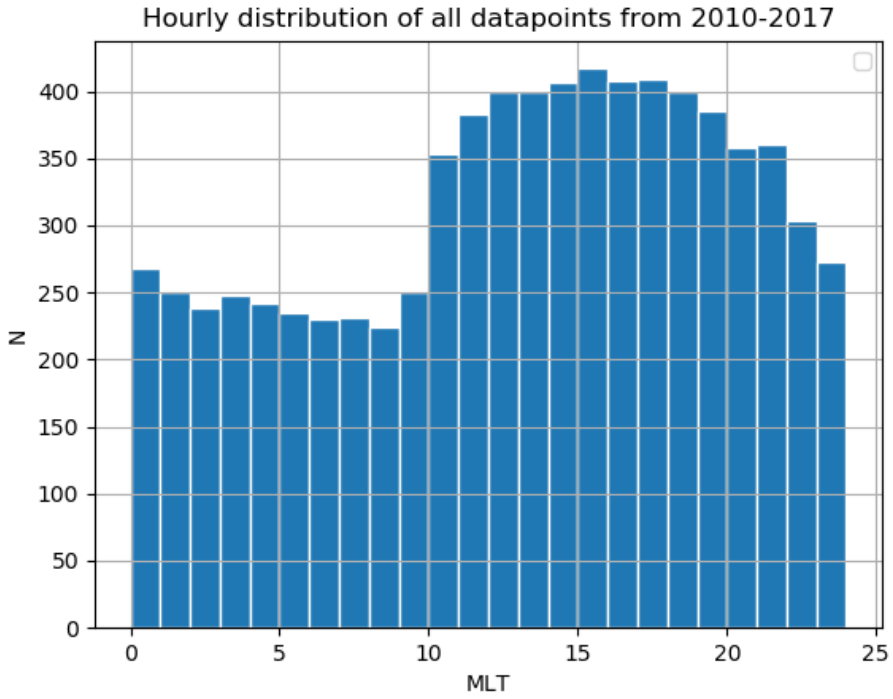


Figure 3.13: Each bracket contains the total amount of data points collected within each hour.

# Chapter 4

# Results

In this chapter the results of our research is presented. The relation between field aligned currents strength and conductance is investigated to determine any possible correlation. The results are shown separately for different MLT, to survey the difference in the relation as a function of time and day, especially to identify any day/night differences. The results are discussed in detail in Chapter 5.

## 4.1 Field-aligned currents and conductance

### 4.1.1 Single day comparisons

Having prepared both the conductances and FACs as described in the previous section, two example days of measurements are presented. Figure 4.1 and Figure 4.2 show the Hall and Pedersen conductances for one full day each, together with the FAC in the bottom panels.

Figure 4.1 shows negative FAC activity (i.e. current flowing into the ionosphere) that occurs simultaneously with an increase in both Hall and Pedersen conductance at roughly 0200 UTC. Figure 4.2 shows a similar kind of activity between 2000 UTC and 2300 UTC. This is the kind of relationship that we anticipate based on the work by Robinson et al. Although a good correlation might be visible in these results, these are only two carefully selected days. To study this correlation in a statistical fashion all of the data must be examined simultaneously.

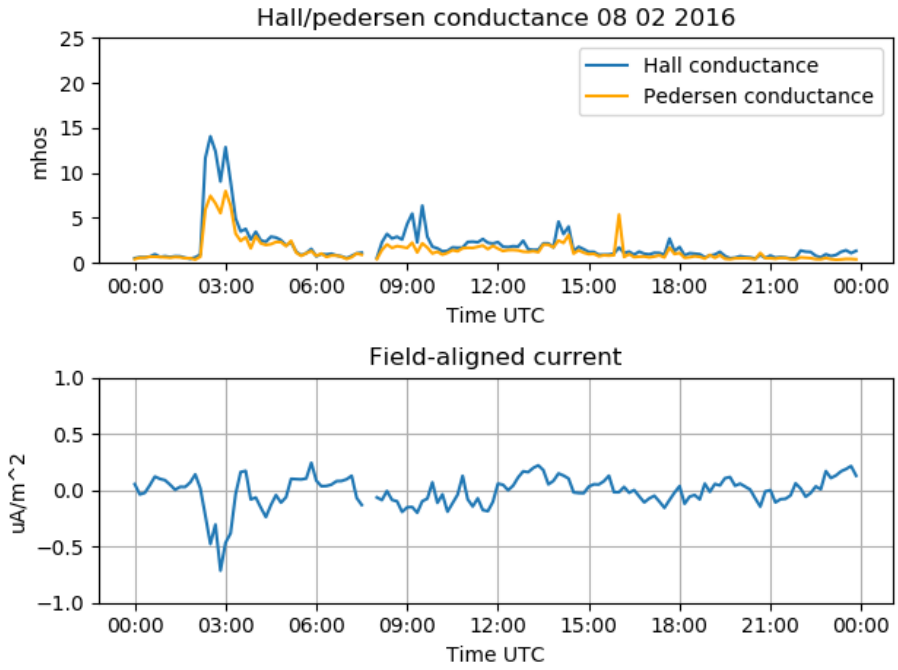


Figure 4.1: The Hall and Pedersen conductance above and field-aligned current below for 8.2.2016

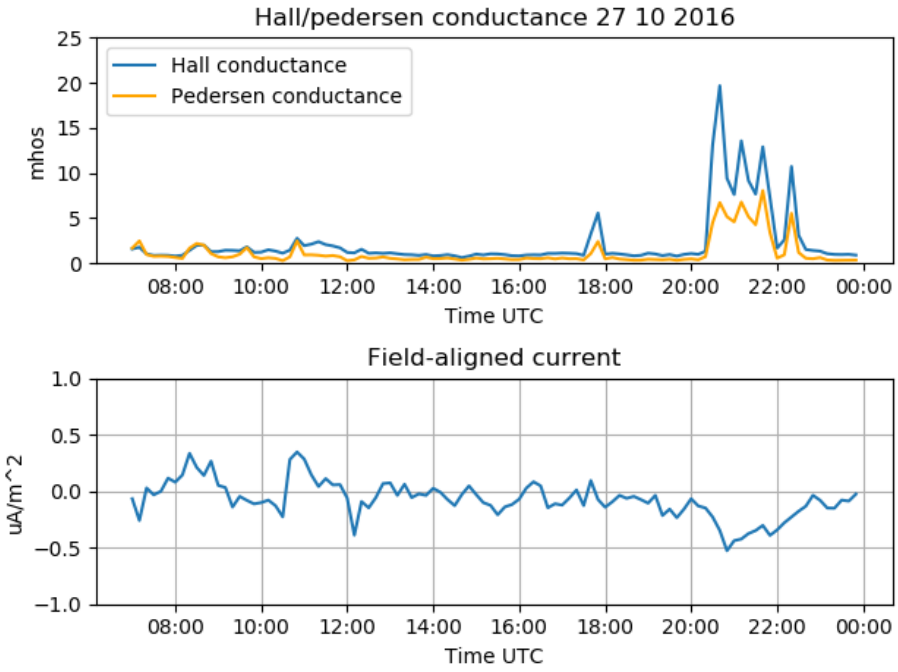


Figure 4.2: The Hall and Pedersen conductance above and field-aligned current below for 27.10.2016

### 4.1.2 Exception days

Section 4.1.1 showed two case studies where local values for conductance and FAC are well correlated. Here it is shown that this is not always the case, hence the necessity of doing a large statistical analysis. This section showcases a few days where an extreme event appears in one of the experiments with no correlating activity appearing in the other. Plausible explanations for these events are presented in Chapter 5, and although this is not the main focus of this thesis their inclusion is still deemed relevant as it points to interesting effects and limitations in our methodology. Figure 4.3 show spiking activity in the conductance while the FAC fluctuates around 0 $\mu A/m^2$. Figure 4.4 and Figure 4.5 show strong FAC activity, and no simultaneous activity in the conductance.

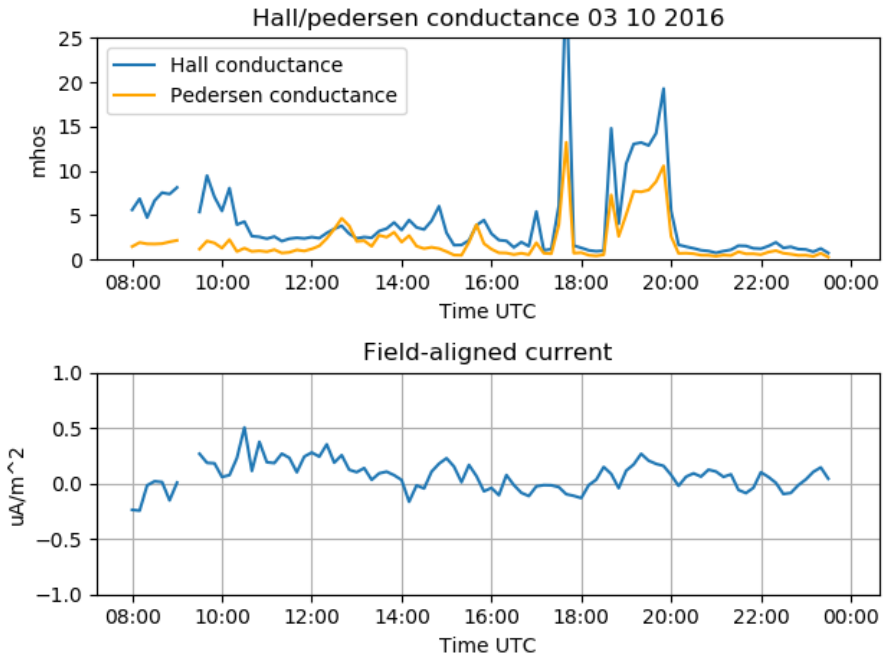


Figure 4.3: 3.10.2016 Spiking conductance at 1730 UTC followed by prolonged high conductance, but no simultaneous FAC activity.

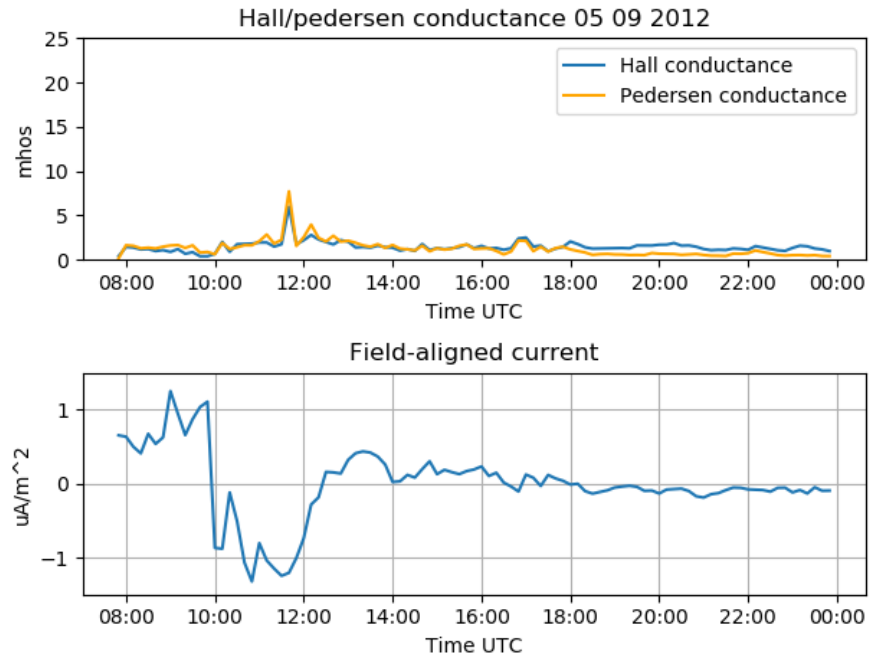


Figure 4.4: 5.9.2012 Strong FAC between 08 UTC and 12 UTC first positive then negative with only one small increase in conductance.

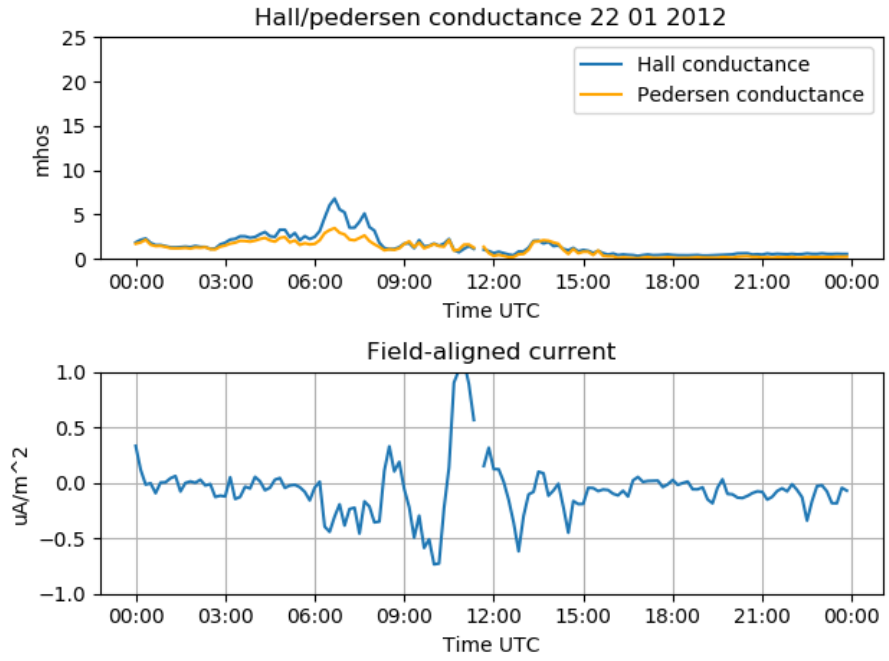


Figure 4.5: 22.1.2012 Small onset of FAC with simultaneous conductance increase between 06 UTC and 08 UTC, with strong and fluctuating FAC during later hours, with no corresponding conductance.

## 4.2 The total data-set

To first get an overview over the total amount of data, all of the unsorted corresponding measurements of conductance and FAC are shown in one scatterplot. In Figure 4.6 the FAC strength is along the x-axis and the Hall and Pedersen conductance is along the y-axis. Each dot represents the corresponding readings for a 10 minute interval. As the figure shows there is a large spread in the data. Most of the data is centered around weak FAC which makes it difficult to see any clear trends.

To identify any correlations that might exist, the data is binned according to FAC values to make the histograms shown in Figure 4.7. Each bin is $0.10\mu A/m^2$ wide. The average conductance for each bin is shown, with the standard error of the mean presented for each point. Most of the readings are in the range of $\pm 0.10\mu A/m^2$, with 4403 points out of the total 7670 falling between these values, which corresponding to 57.4%. These values are represented by the two center-most bins in the figures. Bins with fewer than 10 points are excluded.

To identify any potential correlations we study how the average conductance changes as the absolute value of the FAC increases. We therefore preform a linear regression analysis between the average conductance values for positive and negative values of FAC, respectively. The linear results are shown as the two separate lines in each figure. Each point is weighted to the square root of their respective size N to avoid the near 0 averages dominating the slopes completely. The linear fit will have a coefficient that determines how well the data matches a linear fit. A coefficient close to 1 would indicate a near perfect linear correlation. The coefficients for each slope are marked in the figure as negative coefficient and positive coefficient. The negative coefficient does not indicate a negative slope value, but rather the accuracy of the fit for the points with negative FAC values.

To study the MLT-dependence of the fits, the day is then fragmented into intervals of 6 hours. The four intervals go from 0-6 MLT, 6-12, 12-18 and 18-24. Figures 4.8 through 4.11 show histograms, averages and fits for each MLT range in the same layout as Figure 4.7. This covers two periods on the night side and two periods on the day side. Greater resolution would be preferred, but the scarcity of data with stronger FAC during night time hours results in much greater uncertainties or even insufficient number of strong FAC values to determine any correlations.

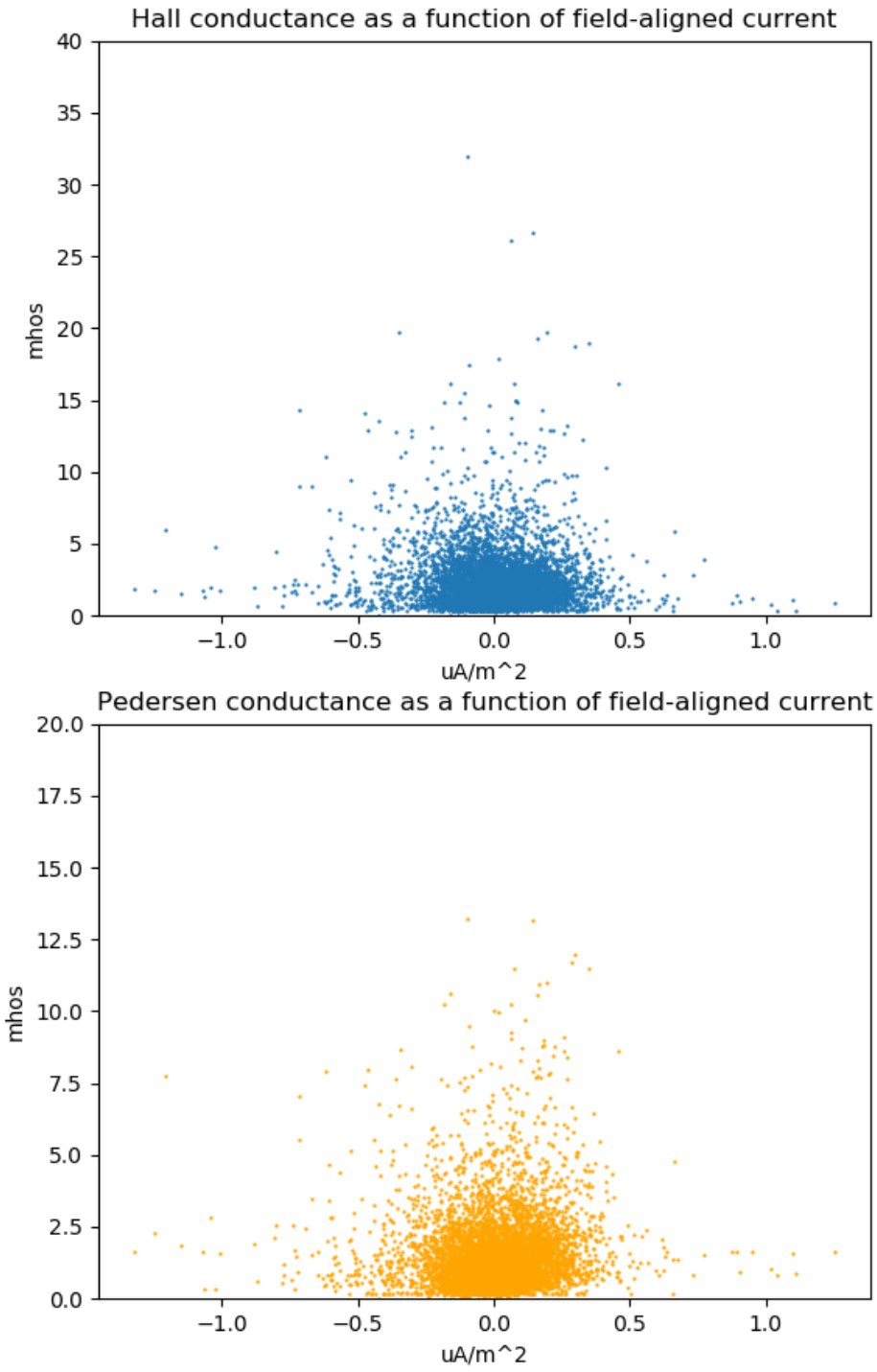


Figure 4.6: The Hall and Pedersen conductance scattered against field-aligned current strength.

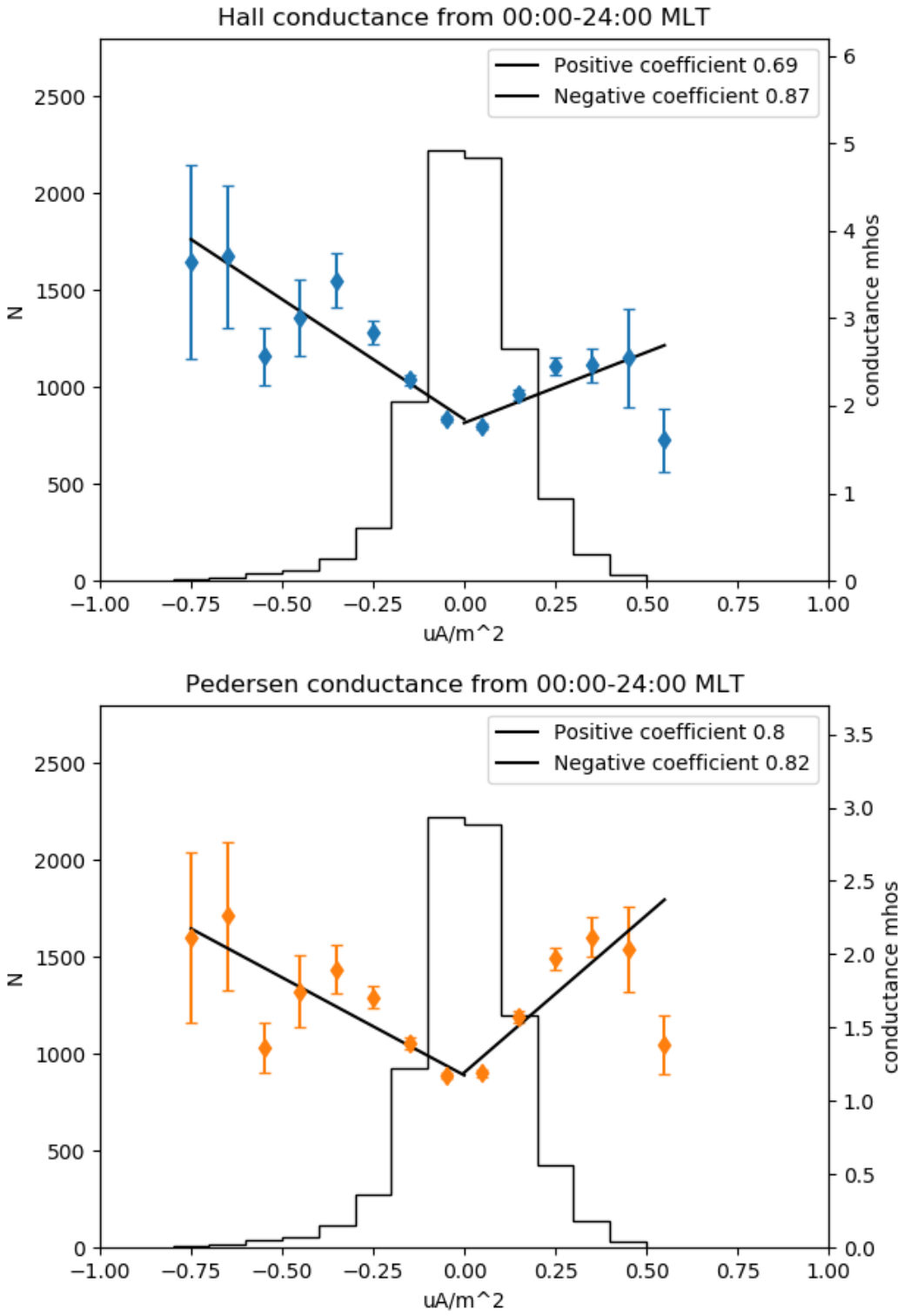


Figure 4.7: Hall and Pedersen conductance sorted into histograms where each bin is 0.1 $\mu A/m^2$ wide. All data present.

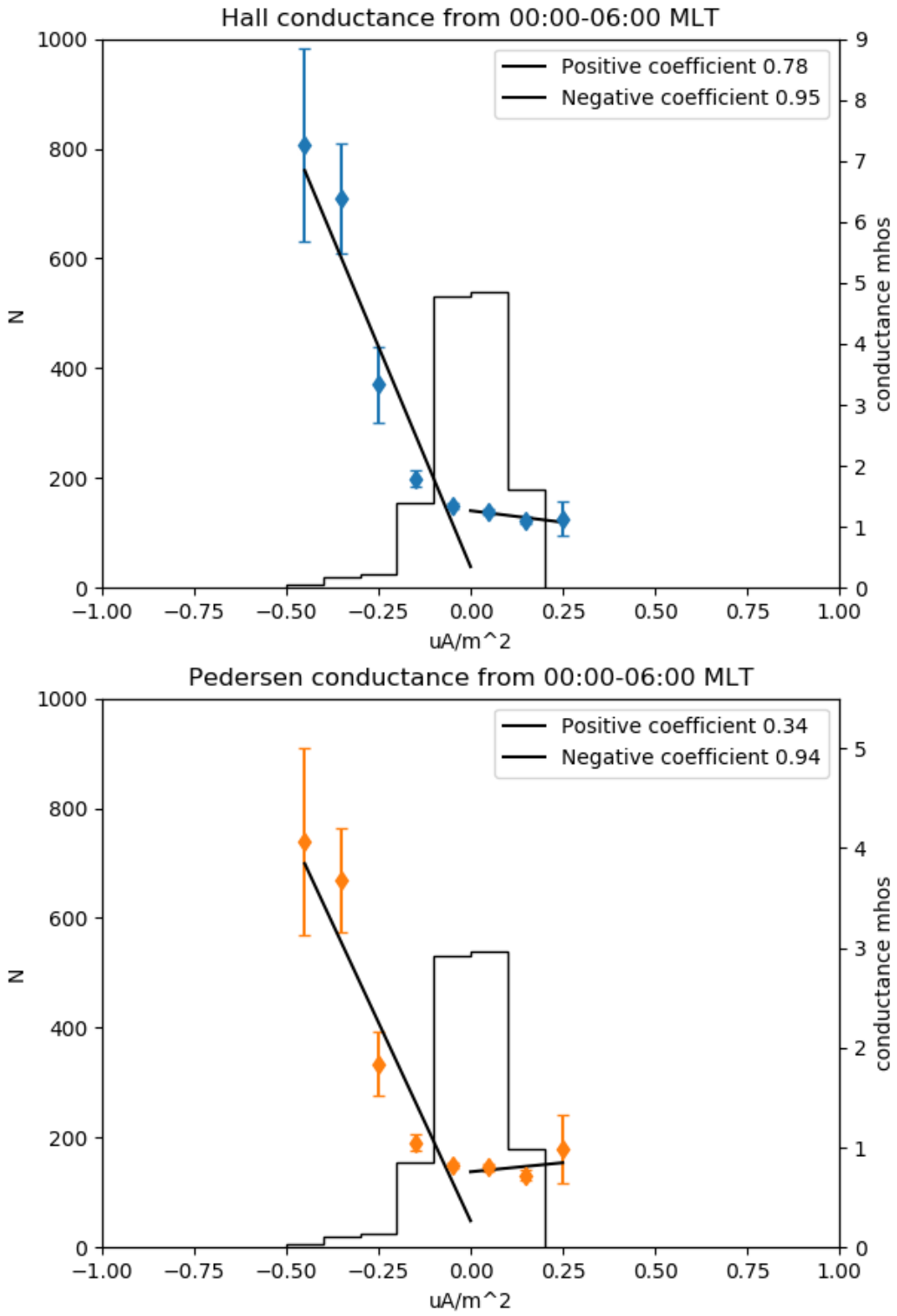


Figure 4.8: Hall and Pedersen conductance sorted into histograms where each bin is 0.1 $\mu A/m^2$ wide. Selected data between 0000 MLT and 0600 MLT.

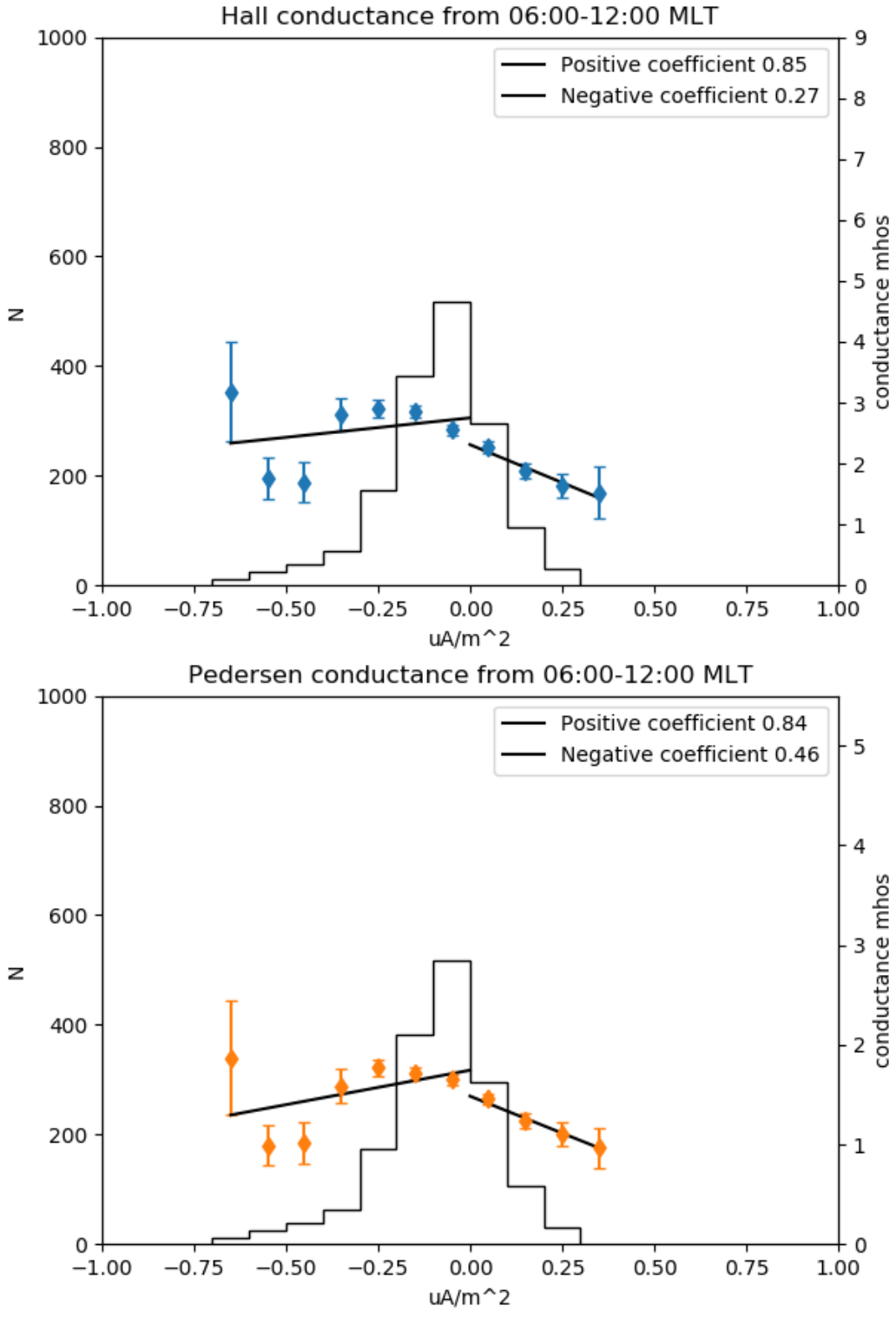


Figure 4.9: Hall and Pedersen conductance sorted into histograms where each bin is 0.1 $\mu A/m^2$ wide. Selected data between 0600 MLT and 1200 MLT.

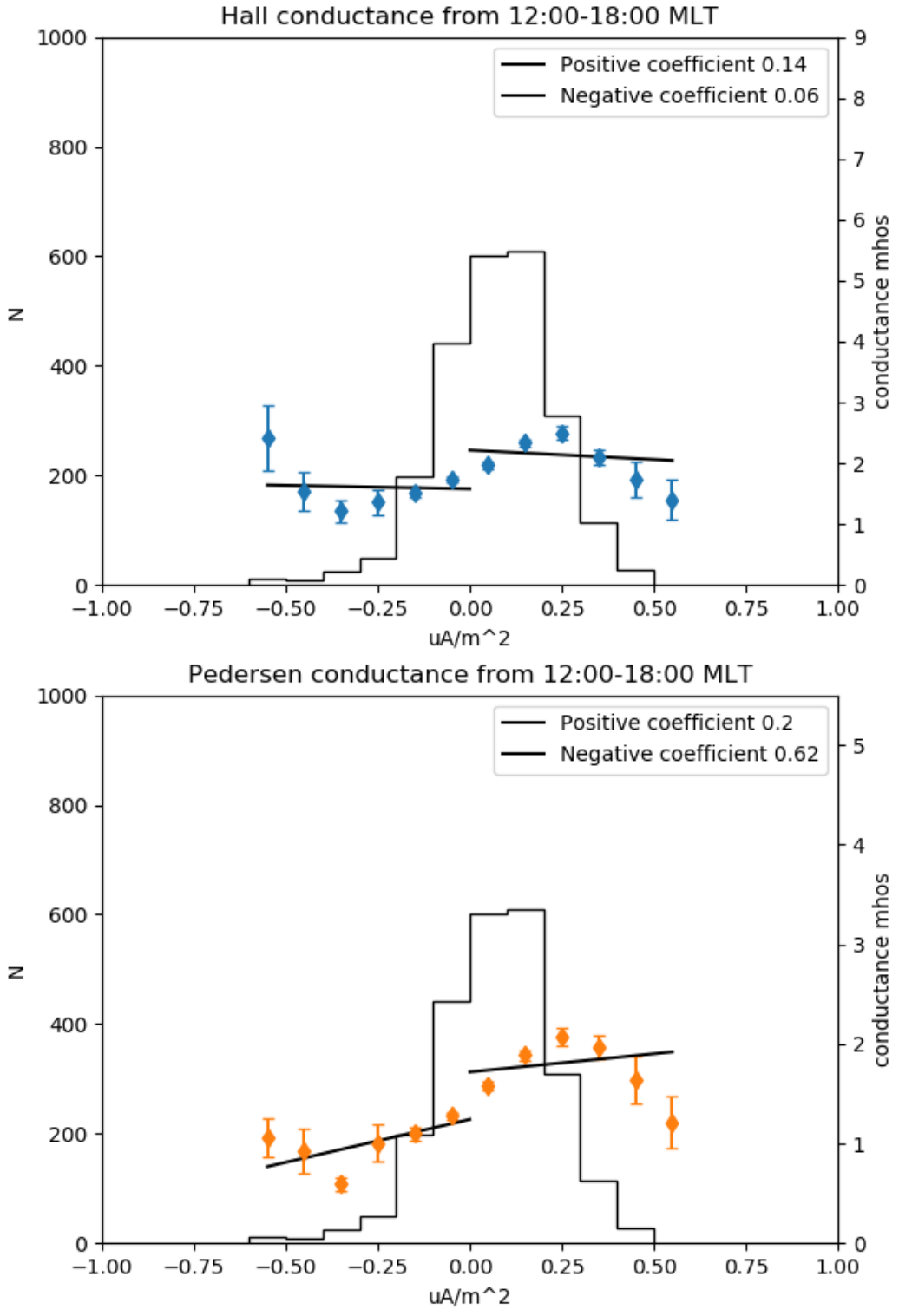


Figure 4.10: Hall and Pedersen conductance sorted into histograms where each bin is 0.1 $\mu A/m^2$ wide. Selected data between 1200 MLT and 1800 MLT.

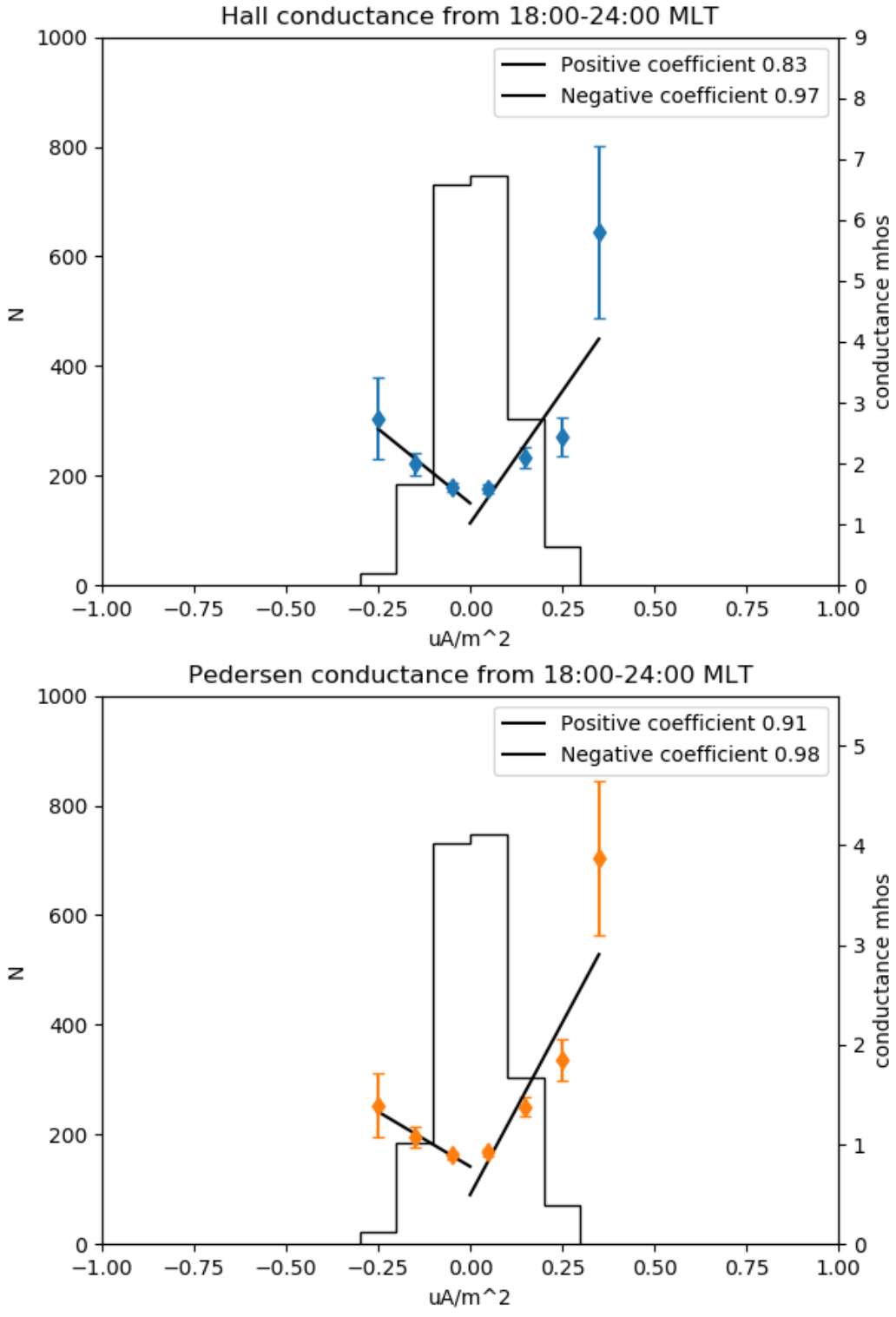


Figure 4.11: Hall and Pedersen conductance sorted into histograms where each bin is 0.1 $\mu A/m^2$ wide. Selected data between 1800 MLT and 2400 MLT.

## 4.3 Variation of FAC with MLT.

Figures 4.8 through 4.11 show that the distribution of observed FAC varies as a function of MLT; for example Figure 4.9 is shifted toward negative values while Figure 4.10 is shifted towards positive values. These trends are explicitly demonstrated in Figure 4.12 which displays the average FAC as a function of MLT.

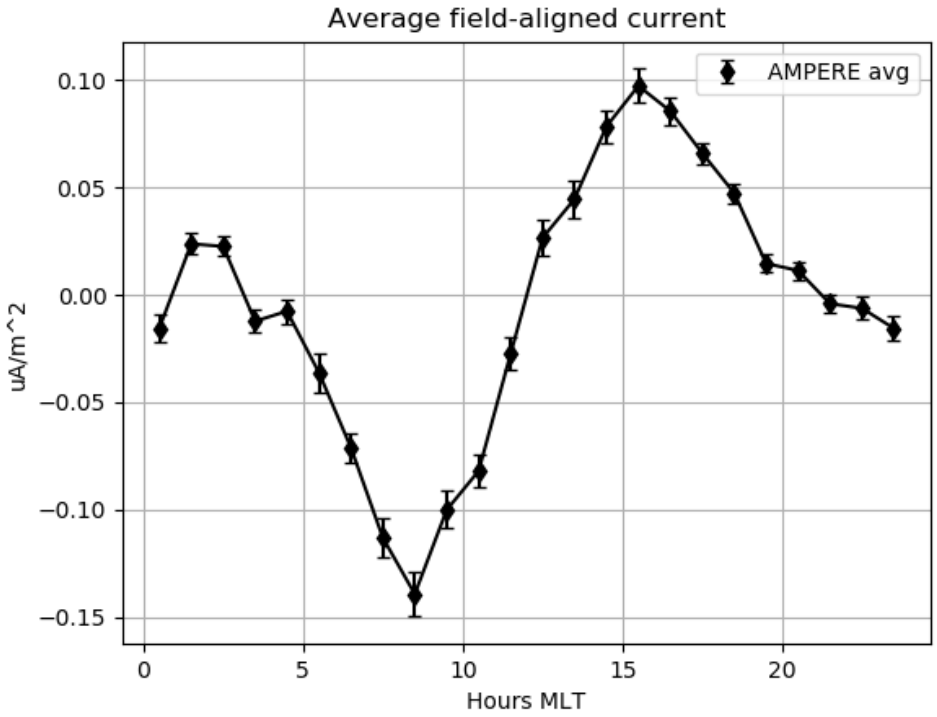


Figure 4.12: Average field-aligned current for every hour.

Between 6 and 12 MLT, average values are negative, while from 12 to 19 MLT the average values are positive. From 19 trough 6 MLT, the average FAC amplitudes are less than $0.05\mu A/m^2$ and display no obvious trend. This is not due to there being is no activity during these hours, only that there is a roughly equal balance between 10 minute interval points with upward currents and downward currents for these MLTs when using large sets of data. Figure 4.13 shows a still of average FAC for a typical solar wind condition. The green circle shows the approximate path of EISCAT. This image will change for some different solar wind conditions, but the regions containing upward and downward currents will remain similar, unless under extreme conditions. The average FAC from Figure 4.12 matches those of Figure 4.13. The variance of the currents we have derived are within expected parameters.

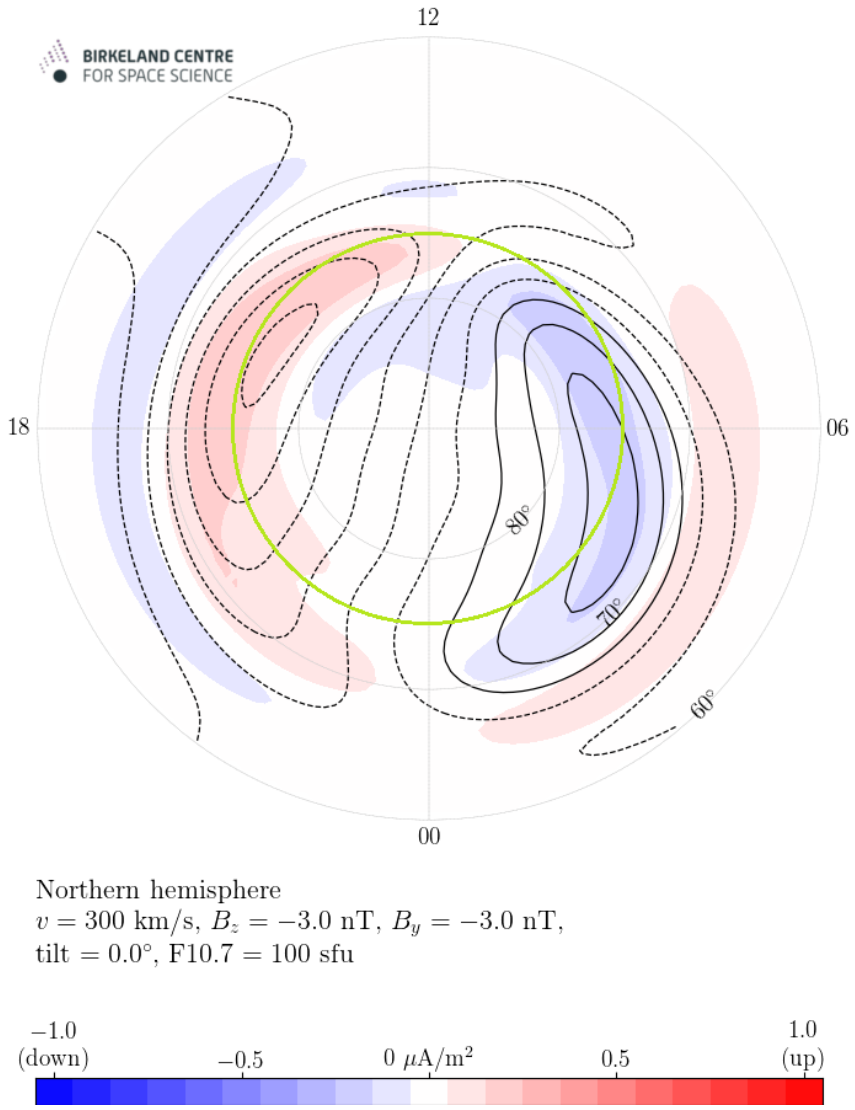


Figure 4.13: A still of average FAC for a typical solar wind condition [28]

## 4.4 The total night-side and single MLT resolution.

From Figures 4.8 to 4.11 it is clear that the correlations are stronger during the night-time hours. To investigate this further we now focus only on these hours. This is shown in Figure 4.14. This figure contains all the MLTs from Figure 4.8 and Figure 4.11.

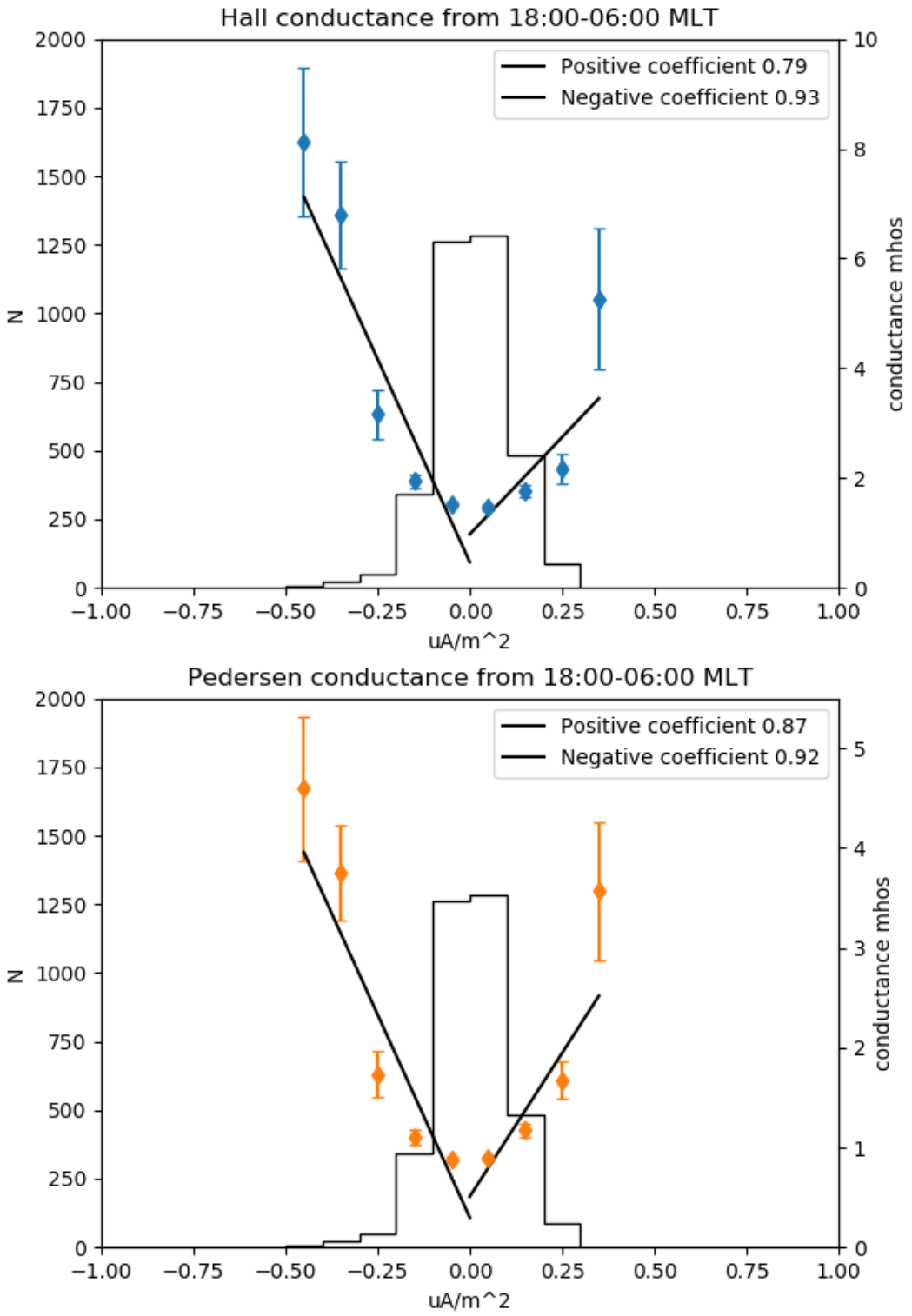


Figure 4.14: All the night-side hours. The average currents might be close to 0 in this region, but as is evident in the figure this is due to an equal balance of up and down currents.

Ideally, we would have liked to be able to present results at greater resolution in order to better compare with the results of Robinson, 2019. Figure 4.15 illustrates the problem in data coverage. In this Figure the results for each MLT individually is shown in a colored grid-chart. The grid has conductance on the y-axis and MLT on the x-axis. Each square is $0.1\mu A/m^2$ tall and 1 hour wide. When doing so the data limitation is removed, so a square containing only a single 10 minute data-point will be visible in the results. The color-bar indicates the average Hall conductance on the right side, and Pedersen conductance on the left. The yellow color shows grid-points with no data. This figure shows that the strongest conductances are found at MLTs within 3-4 hours of midnight. There is an almost complete lack of readings for FAC greater than $\pm 0.5$ during the night-time hours. During the daytime, conductances stay low regardless of FAC activity for all MLT.

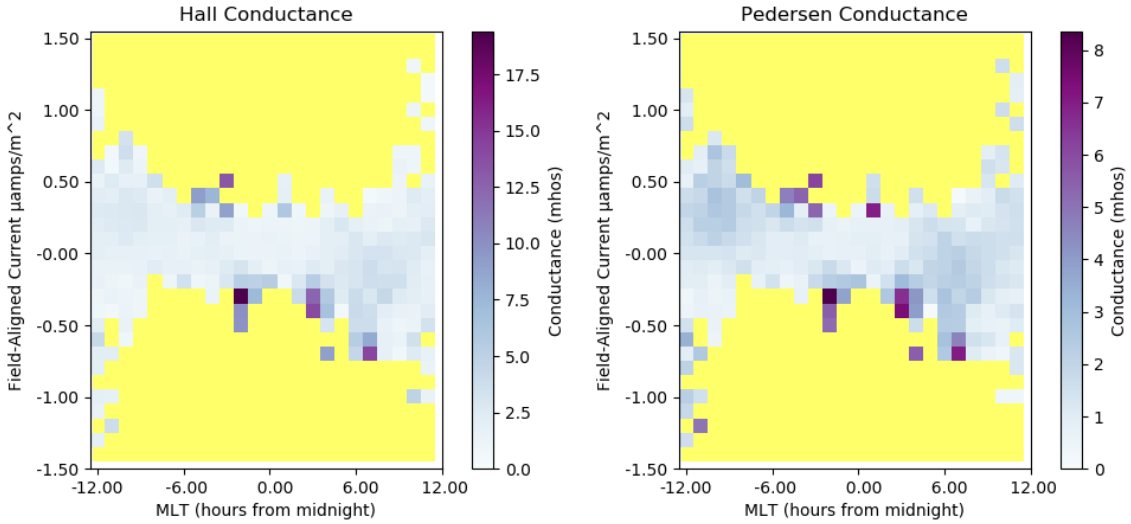


Figure 4.15: Hall and Pedersen conductances in color grid-plot.

# Chapter 5

# Discussion

In this chapter the results found in Chapter 4 are discussed. Correlations found in our research is addressed. A comparison with the Robinson 2019 results is conducted, and an attempt to apply his linear parameter fit equations to our data is done. Comments upon the exception days are also made.

## 5.1 Correlations for different MLT

In section 4.2, Figure 4.7 shows a correlation between FAC and conductance. The correlation is strongest for negative FAC, for which the regression coefficient is 0.87. For positive and low amplitude FAC ($< |0.5|\mu A/m^2$) the correlation is clear, but the trend disappears and average conductances drop for FACs greater than $|0.5|\mu A/m^2$. The Hall conductance averages 2 mhos for weak FAC, and the highest conductance averages up to 4 mhos. The Pedersen conductance is roughly half of the Hall conductance for negative FAC and weak FAC. While the increase in Hall and Pedersen conductances as a function of FAC are similar for negative FACs, the increase in Pedersen conductance is greater than the increase in Hall conductance for positive FAC. When viewing all data simultaneously a correlation can be identified, and we will move on to study the day-side figures and night-side figures separately.

### 5.1.1 Day-side correlation

When reviewing the results shown in Figure 4.9 and Figure 4.10, no clear correlation can be seen between FAC and conductance. The average conductance for the lowest FAC is also higher during the day than the average conductance at the lowest FAC during night time. As seen in Figure 4.15 the most extreme FAC values are between 1000 MLT and 1500

MLT, yet the conductance values for both Hall and Pedersen are not affected. In Robinson 2019 the FAC values on the day-side are low and not correlated with conductance. The result in his case was expected due to Poker Flat, Alaska being south of the auroral oval during the day. During these hours Svalbard is within the auroral oval, so one could expect greater activity in this region. The average FAC for each MLT shown in Figure 4.12 is consistent with the expected values before and after passing through the day-side cusp. Figure 4.13 shows the average FAC for the northern hemisphere during certain solar wind conditions, and we see that our values matches this well.

One reason for the lack of day-side correlation could be inaccuracy in removing the solar contribution, but as mentioned in section 3.3 only a small percentage of the EISCAT Svalbard measurements that we used occurred during sunlit conditions. It is therefore unlikely that our method of removing the solar contribution would have eliminated an otherwise clear correlation.

The more likely reason for lack of clear correlation on the day-side has to do with the Knight relation not being valid there. The FAC are not associated with persistent field-aligned potential drops.

### 5.1.2 Night-side correlation

In contrast to the results for the day-side, the results in Figure 4.14 show a clear correlation between stronger FAC and higher Hall and Pedersen conductance. Both for positive FAC and negative FAC the conductance is correlated. When looking at the night-side in pre midnight and post midnight (Figures 4.8, 4.11) we see that the majority of positive FAC values are found before midnight, and the majority of negative FAC values are found after midnight. In the pre-midnight hours we see only a correlation for negative FAC, but this is due to the lack of strong positive FAC in the relevant hours. Looking back at Figure 4.15 showing the conductance for every MLT, we see that the strongest FAC to occur on the night-side have values around $\pm 0.5 \mu A/m^2$. A possible explanation for the absence of stronger FAC is the high latitude of Svalbard. During the night Svalbard is pole-ward of the active auroral zone so any strong FAC during these hours would be a rarity, since FACs mainly occurs at the borders of open and closed magnetic field lines. For stronger FAC to occur at Svalbard, conditions have to be unusual. We conclude that there is not enough data in this region of time to properly discuss how conductance behaves statistically for stronger FAC.

## 5.2 Comparisons with the Robinson 2019 model

In Statistical relations between auroral electrical condutances and field-aligned currents at high latitudes [2019 Robinson et al], Robinson proposes the following equations describing linear fits between FAC and conductance.

$$\Sigma_P^u = \Sigma_{P0}^u + M_P^u j_{||}^u; \Sigma_P^d = \Sigma_{P0}^d + M_P^d j_{||}^d \tag{5.1a}$$

$$\Sigma_H^u = \Sigma_{H0}^u + M_P^u j_{||}^u; \Sigma_H^d = \Sigma_{H0}^d + M_P^d j_{||}^d \tag{5.1b}$$

Here $\Sigma_P$ and $\Sigma_H$ are the Pedersen and Hall conductance respectively. 'u' and 'd' denote fits to upward and downward currents. $\Sigma_{P0}^{u,d}$ and $\Sigma_{H0}^{u,d}$ are the y-intercepts of the linear fits while $M_P^{u,d}$ and $M_H^{u,d}$ are the corresponding slopes for the Pedersen and Hall conductance respectively. Robinson 2019 find these fits for each MLT based on the data acquired by the Poker Flat Radar and presents a table. The fitting parameters (y-intercepts and slopes) obtained for night-time MLTs are shown in table 5.1. We will use this table and compare to the data derived from the EISCAT Svalbard radar. The comparison is only done for the night-side, as both our results and those of Robinson 2019 do not show statistically significant correlations for the day-side.

| MLT | $\Sigma_{P0}^d$ | $M_P^d$ | $\Sigma_{P0}^u$ | $M_P^u$ | $\Sigma_{H0}^d$ | $M_H^d$ | $\Sigma_{H0}^u$ | $M_H^u$ |
|---|---|---|---|---|---|---|---|---|
| 0 | 4.80 | -8.38 | 5.50 | 11.23 | 8.89 | -11.36 | 11.37 | 20.57 |
| 1 | 4.66 | -8.85 | 5.57 | 11.67 | 8.61 | -12.63 | 11.85 | 23.27 |
| 2 | 4.51 | -9.05 | 5.62 | 11.85 | 8.21 | -13.73 | 12.11 | 25.54 |
| 3 | 4.36 | -8.95 | 5.63 | 11.71 | 7.80 | -14.54 | 12.14 | 27.25 |
| 4 | 4.25 | -8.52 | 5.60 | 11.21 | 7.44 | -14.97 | 11.91 | 28.30 |
| 5 | 4.19 | -7.75 | 5.51 | 10.32 | 7.23 | -14.92 | 11.43 | 28.57 |
| | | | | | | | | |
| 19 | 4.73 | -4.33 | 5.07 | 7.56 | 6.76 | -5.39 | 7.47 | 5.23 |
| 20 | 4.85 | -5.13 | 5.14 | 8.28 | 7.66 | -6.35 | 8.27 | 8.05 |
| 21 | 4.92 | -6.01 | 5.22 | 9.06 | 8.37 | -7.45 | 9.12 | 11.15 |
| 22 | 4.94 | -6.88 | 5.31 | 9.85 | 8.81 | -8.69 | 9.96 | 14.36 |
| 23 | 4.90 | -7.70 | 5.40 | 10.59 | 8.97 | -10.01 | 10.73 | 17.55 |

Table 5.1: Total hours of experiments for each month and year for the 2010-2017 period.

Ideally we would have liked to produce a similar table to find the y-intercepts and slopes at Svalbard for each MLT. However as illustrated in Figure 4.15 the low number of strong FAC events does not allow a meaningful regression analysis comparison for individual MLTs. We will therefore compare the results of Robinson 2019 to the y-intercept and slopes of our total night-side analysis. Table 5.1 shows that the y-intercepts and slopes at poker flat change in relation to being pre midnight or post midnight. For this reason

slopes and y-intercepts for 6 hour periods prior to and post midnight are also provided. The parameters being compared are therefore the linear regression lines from Figures 4.8, 4.11 and 4.14.

EISCAT Svalbard measurements

| MLT | $\Sigma^d_{P0}$ | $M^d_P$ | $\Sigma^u_{P0}$ | $M^u_P$ | $\Sigma^d_{H0}$ | $M^d_H$ | $\Sigma^u_{H0}$ | $M^u_H$ | $P_0$ | $H_0$ |
|---|---|---|---|---|---|---|---|---|---|---|
| 00-06 | 0.36 | -7.95 | 0.76 | -0.36 | 0.35 | -14.44 | 1.26 | -0.76 | 0.80 | 1.30 |
| 18-24 | 0.77 | -2.20 | 0.49 | 6.89 | 1.35 | -4.88 | 1.02 | 8.64 | 0.91 | 1.60 |
| 18-06 | 0.30 | -8.13 | 0.51 | 5.74 | 0.47 | -14.78 | 0.97 | 7.06 | 0.88 | 1.49 |

Poker Flat measurements

| MLT | $\Sigma^d_{P0}$ | $M^d_P$ | $\Sigma^u_{P0}$ | $M^u_P$ | $\Sigma^d_{H0}$ | $M^d_H$ | $\Sigma^u_{H0}$ | $M^u_H$ | - | - |
|---|---|---|---|---|---|---|---|---|---|---|
| 00-06 | 4.46 | -8.53 | 5.57 | 11.33 | 8.03 | -13.69 | 11.80 | 25.58 | - | - |
| 18-24 | 4.82 | -5.82 | 5.19 | 8.71 | 7.73 | -7.01 | 8.82 | 9.86 | - | - |
| 18-06 | 4.64 | -7.10 | 5.38 | 10.02 | 7.88 | -10.39 | 10.26 | 17.72 | - | - |

Table 5.2: Slopes and y-intercepts for figures 4.8, 4.11 and 4.14 above. Averaged Poker Flat slopes and y-intercepts below.

Table 5.2 shows the slopes derived from the Svalbard data together with the averaged slopes and y-intercepts from the Poker Flat data. Some of the $M^{u,d}_{P,H}$ values create $\Sigma^{u,d}_{P,H}$ values that are far below the measured values of conductance at $\pm 0.05 \mu A/m^2$. $P_0$ and $H_0$ is therefore included. which represent the measured values. This does highlight a weakness with the linear approach. $M^u$ for 00-06 MLT and $M^d$ for 18-24MLT is marked with red. These values are calculated using only 3 points of data. The linear coefficient might still be large and indicate that the slope is accurate, but these results are based of values with few strong FAC readings. Note that while the EISCAT Svalbard numbers are derived directly from the radar measurements, the Poker Flat numbers are averaged from Table 5.1. The most striking difference is that the y-intercepts are at much lower values at Svalbard than at Poker Flat. The measurements derived from the EISCAT Svalbard have the y-intercepts in the range of 1.3-1.6 mhos for Hall conductance and 0.8-0.9 mhos for Pedersen conductance, while the y-intercepts derived from Poker Flat has these values are ranging from 7.7-11.8 mhos and 4.4-5.6 mhos respectively. In the EISCAT Svalbard data $P_0$ is slightly greater from 18-24 MLT than from 0-06 MLT. This is also the case in the Poker Flat data. For Hall conductance EISCAT stronger $P_0$ from 18-24 MLT than from 00-06 MLT. For Poker flat the y-intercepts for Hall conductance are stronger from 00-06 MLT for both up and down currents.

The lower y-intercepts are likely due to overall lower levels of conductance at Svalbard and in the northern polar cap in general. The slopes are therefore of greater interest since they would compare our correlation results to those of Robinson 2019 regardless of the calmer averages. The $M^u_{P,H}$ from 00-06 MLT and $M^d_{P,H}$ from 18-24 MLT at Svalbard are

unfortunately highly uncertain due to the lack of sufficient relevant data for these hours. The rest of the slope values can still be meaningfully compared though. $M_P^d$ for 00-06 MLT are very similar, with EISCAT being 7% larger than Poker Flat. The $M_H^d$ show a similar situation. The $M_{P,H}^u$ from 18-24 MLT are also comparable, with Poker Flat giving 20% higher values than EISCAT. When looking at the whole night-side (18-06 MLT) $M_{P,H}^d$ remain relatively close in values, but for $M_{P,H}^u$ the Poker Flat values are more than twice of those from EISCAT.

## 5.3 The significance of the geomagnetic location of Svalbard

Figures 4.9 and 4.10 in section 4.2 show that there is no correlation between FAC and conductance during day-time at Svalbard. The Knight-relation [1973] predicts a relationship between FAC and electric potential in the ionosphere, and Robinson [2002] proposed a relationship between particle precipitation and conductance. As mentioned previously the Knight relations is not valid on the day-side. Our results show no correlation between conductance and FAC for the MLT during which particle precipitation is most likely at Svalbard.

Particle precipitation during night-time does occur at Svalbard. It is however infrequent, since it requires quite unusual conditions to be met. For particle precipitation to occur at night, the polar cap must first be contracted from low activity levels, and then expand across Svalbard as activity increases. Svalbard also must be in the correct MLT position when such an event occurs. This will cause the auroral oval to move equator-ward over Svalbard, with related particle precipitation. It is rare for the auroral oval to be this far north on the night-side, and this explains the lack of many strong FAC events during these MLTs in the EISCAT data. Whenever magnetospheric activity occurs on the night-side, it is likely that Svalbard is too far north to measure it. Thus both EISCAT and AMPERE will mostly record background readings of no particular significance. To get a more accurate picture of the correlation between strong FAC and high ionospheric conductance more data would have to be acquired.

## 5.4 Case studies

In section 4.1.2 three days were presented where there is great activity in either the FAC or the conductance, yet no simultaneous activity in the other parameter. In this section a case by case study of these days will be presented. Figure 4.4 and Figure 4.5 both

have strong FAC activity during the daytime hours. The statistical analysis show no clear correlations for these hours. Given the extremity of the events and potential future studies they warrant closer examination.

Figure 4.3 shows great activity in conductance from 1800 UTC to 2000 UTC, with only weak FAC occurring simultaneously. Reviewing this specific time-frame in a broader perspective shows that there is indeed FAC activity in the neighbouring regions. At the time of the highest conductance, EISCAT Svalbard is located in the center of an upward FAC and a downward FAC structure. It is therefore well possible that this conductance is indeed associated with strong FAC, but the method of averaging to estimate the FAC in the immediate area of the RADAR is insufficient to account for the total activity in the region. A plot of the AMPERE interpolated data is shown in Figure 5.1. A downward current is visible south-east of Svalbard, and an upward current north-west of Svalbard. Examining the relation of conductance with strong FAC activity in a larger region surrounding the radar measurement volume would be an interesting subject for a future study.

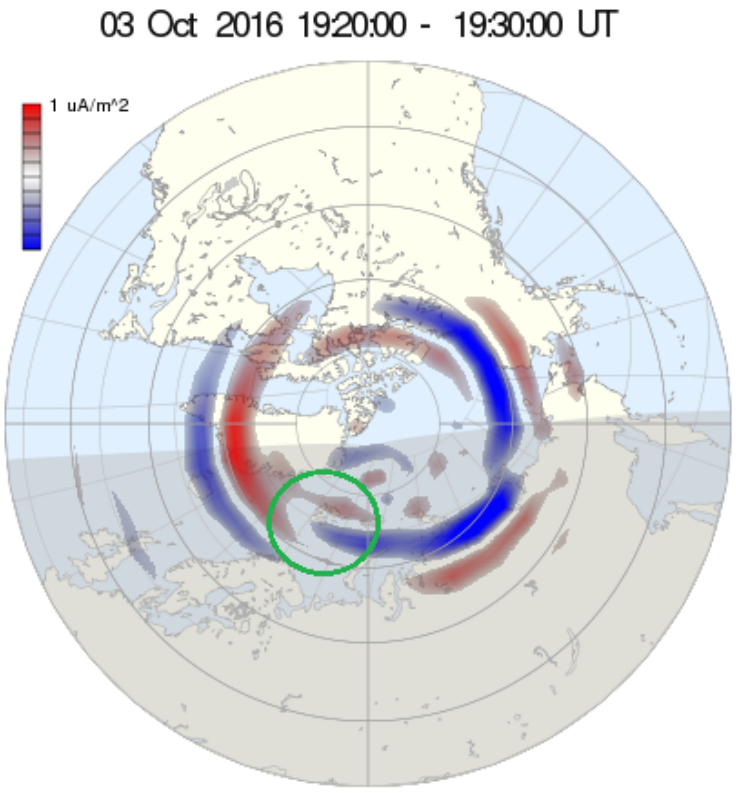


Figure 5.1: AMPERE data showing up and down FAC for 3.10.2016 at 1930 UTC, close to the peak shown in Figure 4.3. Svalbard in encircled in green.

Figure 4.4 shows the Pedersen and Hall conductance together with the AMPERE derived

FAC for 5.9.2012. Svalbard is below a strong downward FAC, but there is no simultaneous increase in conductance. Whether this event produced day-side auroras in the relevant period is unknown, since no relevant all-sky data could be acquired. This event happened in September, during hours where the sun would be present on the sky. All the strong FAC activity happens between 10-13 UTC ( 12-15 MLT). In these hours the statistical analysis showed no correlation between conductance and MLT, so this one day measurement shows that even for short extreme events this remains the case.

The case study of 22 January 2012 (Figure 4.5) does produce some interesting results. In the FAC curve a downward onset is visible close to 0600 UTC that has a simultaneous jump in both Hall and Pedersen conductance. The FAC is then reduced, with the conductance dropping in accordance. At 0900 strong geomagnetic activity begins, with the FAC exhibiting strong changes between $-0.7\mu A/m^2$ and $+1.1\mu A/m^2$. The conductance however remains at background levels. The oscillations last until roughly 1300 UTC, where the FAC also returns to low values. Figure 5.2 shows the All-sky aurora camera data parallel to the AMPERE and EISCAT derived data, and there is strong auroras present during the high activity hours. Figure 5.4 shows the FAC map produced by AMPERE for 1700 UTC and it is clear that the storm is still active, but the activity is now equator-ward of Svalbard. Looking at the Dst-Index for the January 2012, the onset and the storm development is clear (Figure 5.3). This case is interesting because it does show an initial correlation between conductance, aurora and FAC during the early morning hours, but during midday the conductance is unaffected even though strong auroras are detected. This suggests that the correlation between conductance and FAC is entirely restricted to the night-side, and might be independent of auroras in general, or that the auroras on the day-side are different from the night-side aurora. (maybe references to studies being done about this) This behaviour is reflected in the larger data set, which shows that that strong FAC during midday hours is more common at Svalbard, but it does not produce strong Hall and Pedersen conductances.

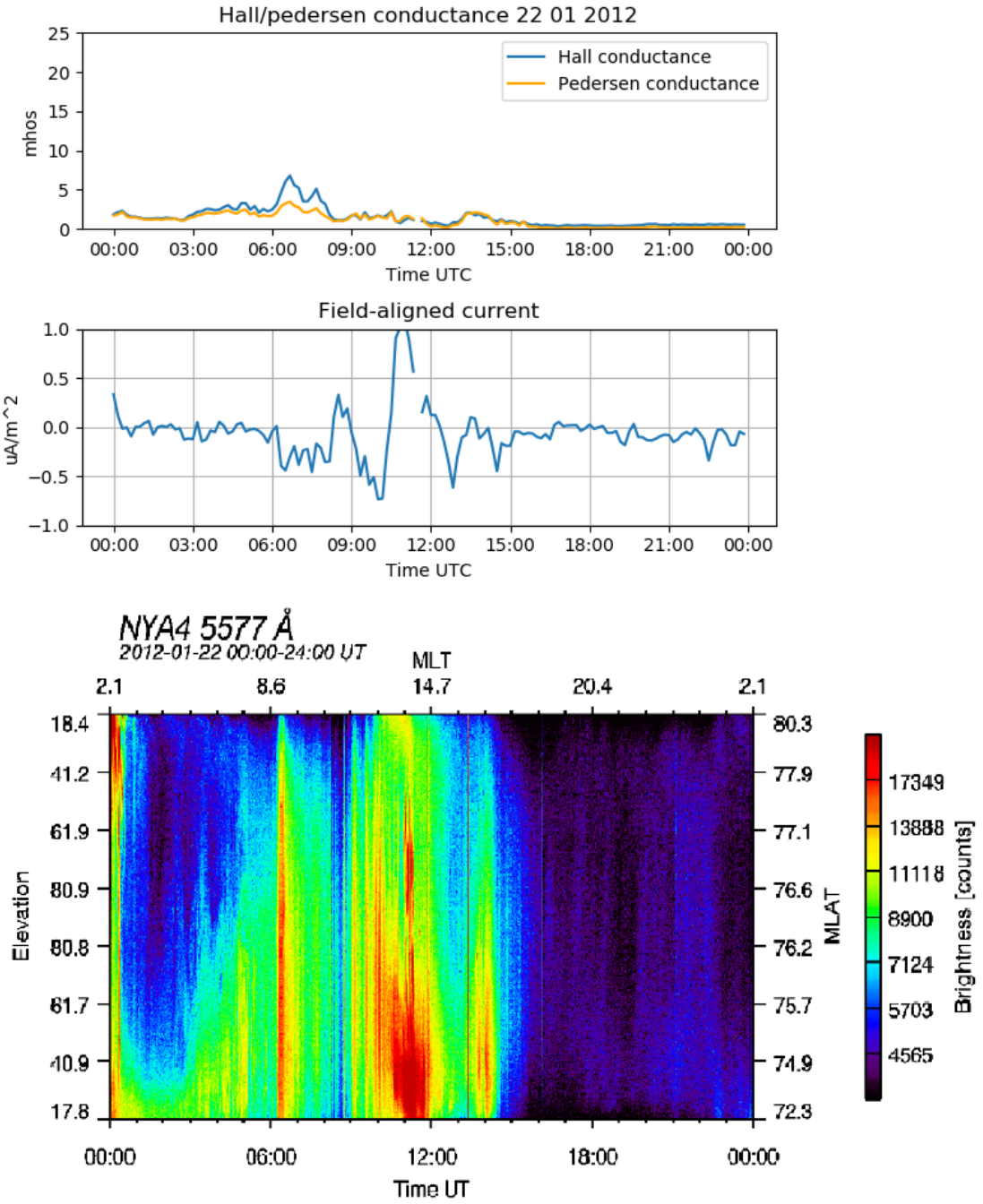


Figure 5.2: Aurora all-sky camera data [29] for 22.01.2012 synchronized with the AMPERE derived FAC and EISCAT Svalbard measured conductance.

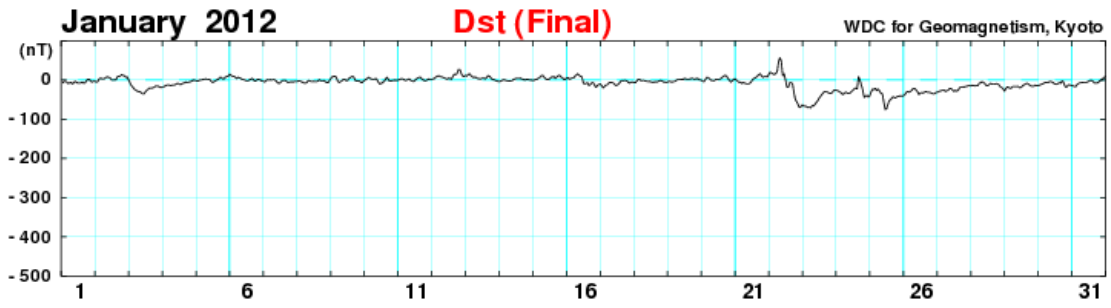


Figure 5.3: Dst-index for January 2012. The sub-storm begins at 22.01, with the recovery period lasting several days.

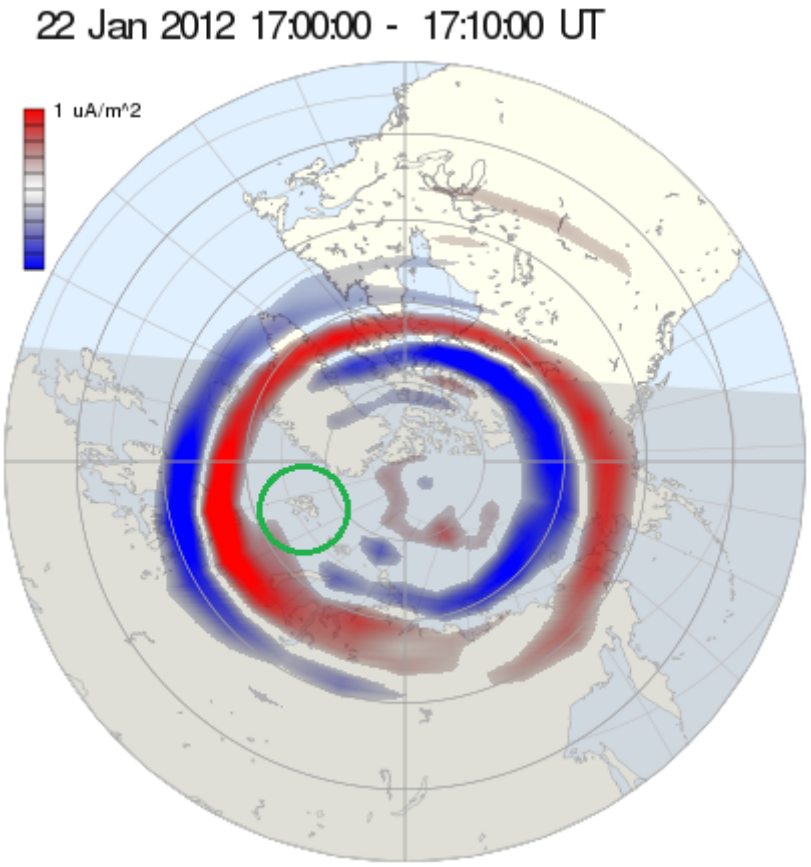


Figure 5.4: AMPERE plot for 22.01.2012 at 1700 UTC. Svalbard in the middle of the green circle.

# Chapter 6

# Conclusion and outlook

In this thesis the relationship between FACs in the high altitude ionosphere and the Hall and Pedersen conductance in the lower ionosphere above Svalbard, Norway was investigated. This is an extension of work presented in Robinson, 2019 which studied this same relationship over Alaska USA. It also follows work that has studied the correlation between FAC and other ionospheric properties over several decades [Knight, etc]. The examination of a relationship between conductance and the present FAC during the night-time hours has been the main interest in this study. The present work is based on an analytical approach which compares the FAC and conductance derived from two separate experiments. The FAC are derived from the AMPERE experiment, which is magnetic field variations measured by the iridium communications satellite constellation. The Hall and Pedersen conductances are derived from the measurements done with the EISCAT Svalbard incoherent scatter radar.

The results obtained in this work is presented in Chapter 4 and discussed in detail in Chapter 5. For the night-side encompassing 6 hours before and after midnight, a correlation between FAC and Hall and Pedersen conductance was found. The amount of data present in our study was insufficient to provide a credible estimate of how this correlation depends on MLT. For the 12 hours encompassing the day-side, no clear correlation was found. When comparing to the results of Robinson, 2019 we found that conditions on Svalbard are in general much calmer, with the y-intercept conductance values in general being 4-7 times weaker than those found at Poker Flat for both Hall and Pedersen conductances. The fit slopes derived from Svalbard are closer to those derived from PFISR compared to the y-intercepts, and ranged from 1.1-3 times smaller. At PFISR, Robinson found that the correlation between FAC and conductance was stronger for positive values of FAC. At Svalbard we found that the correlation was stronger for negative values of FAC. This may be due to insufficient data containing positive FAC, but may also be a

product of different ionospheric conditions at Svalbard. A case study of 22.01.2012 showed no day-side correlation between FAC and conductance despite the presence of auroras for the relevant hours. The model described in Robinson 2019 is based on the assumption that FAC are correlated with aurorally-produced ionospheric conductance. Our results have indicated that this may no be universally true for day-side auroras. Understanding the relation between FAC, particle precipitation and conductances in the day-side cusp area is an active area of research[30][31].

This thesis presents results that provide information about the relationship between FAC and Hall/Pedersen conductance in the immediate surroundings of Svalbard Norway. The geomagnetic position of Svalbard provided us an opportunity to study this relationship on the day-side and in the presence of strong day-side auroras. The scarcity of data for strong FAC on the night-side does put some limit on our ability to study the night-side relationship completely. There are several different approaches that could be taken to further increase our understanding of this relationship. Our study encompass the period of 2010-2017. In the future more data will be available from the EISCAT Svalbard radar that can be used in a similar study, so the repetition of this study in the future would provide a better understanding of the relationship we studied. Alternatively using a different radar for the ionospheric profile can be done. PFISR has an invariant latitude of approximately 65.9°north and sees almost exclusively heavy night-side activity, while EISCAT Svalbard is at 75.18°and sees far less extreme FAC on the night-side, but did provide the opportunity to study the day-side activity. Using a radar somewhere in between these invariant latitudes might provide the same opportunity to study day-side activity, but be more inclined towards stronger night-side activity levels. Conducting a similar study for the southern hemisphere would also be an interesting addition to our understanding the global ionospheric profile.

# Bibliography


[1] Brekke A., Egeland A., *Nordlyset: Kulturarv og vitenskap* Oslo : Groendahl Dreyer, 1994

[2] Hearne, Samuel. *A Journey to the Northern Ocean: A journey from Prince of Wales Hudson's Bay to the Northern Ocean in the years 1769, 1770, 1771, 1772.* Toronto: The MacMillan Company of Canada, Richard Glover ed. 1958.

[3] Halley E., 'An account of the late surprising appearance of light seen in the air, on the sixth of March last, with an attempt to explain the principal phenomenal thereof, As it was laid before the Royal Society by Edmund Halley, J.V.D., Savilian Professor of Geometry, Oxon and Reg. Soc. Secr', *Phil. Trans. R. Soc. Lond.* 29, 406-428, 1716

[4] Egeland A., *Kr. Birkeland: mennesket og forskeren.* Oslo : Norges banks seddeltrykkeri, 1994

[5] Birkeland K., Sur les rayons cathodiques sous l'action des forces magnétiques inteses. *Archives des sciences physiques et naturelles* 36me periode **T.33** (1896) 297-309.

[6] Birkeland, K., *The Norwegian Aurora Polaris Expedition 1902-1903, Vol. 1* , H. Aschehoug and co., Christiania 1908 and 1913

[7] Neugebauer M. and Snyder C. W., Solar Plasma Experiment. **Science** 138 (3545): 1095–1097, 1962

[8] Dungey J. W., Interplanetary Magnetic Field and the Auroral Zones *Physical Review Letters* vol. 6, Issue 2, pp. 47-48. 1961

[9] Alfvén H., Existence of electromagnetic-hydrodynamic waves. *Nature* 150 (3805): 405-406.

[10] Knight. S. Parallel electrix fields, *Planetary and Space Science* , 21, 741-750, 1972

[11] Robinson, R., Vondrak R., Miller, K., Dabbs, T. and Hardy, D.: On calculating ionospheric conductances from the flux and energy of precipitating electrons. *J. Geophys. Res.* 92, 2565, 1987

[12] Lumerzheim, D., Rees, M.H, Craven, J., and Frank, L.: Ionospheric conductances derived from spectral auroral images *J. Atmos. Terr: Phys.* , 51, 281, 1991

[13] Ridley A. J., Gombosi T. I., and DeZeeuw D. L. Ionospheric control of the magnetosphere: conductance *Annales Geophysicae* 22: 567-584 2004

[14] Robinson, R., Anderson, B., and Zanetti, L. (2019). AMPERE-Derived Electrodynamic Parameters of the High Latitude Ionosphere (ADELPHI). *Geophysical Research Abstracts*, 21(EGU2019-3577).

[15] EISCAT Radar. Svalbard, Norway. https://www.eiscat.se/about/sites/eiscat-svalbard-radar

[16] Anderson, B. J., Korth, H., Waters, C. L., Green, D. L., and Stauning, P. (2008). Statistical Birkeland current distributions from magnetic field observations by the Iridium constellation. *Annales Geophysicae*, 26(3), 671–687.

[17] Active Magnetosphere and Planetary Electrodynamics Response Experiment http://ampere.jhuapl.edu

[18] Baumjohann W. and Treumann R. A. *Basic space plasma physics.* Imperial College Press, revised edition, 2012.

[19] Le, G., J. A. Slavin, and R. J. Strangeway. Space Technology 5 observations of the imbalance of regions 1 and 2 field-aligned currents and its implication to the cross-polar cap Pedersen currents, *J. Geophys. Res.* , 115, A07202 2010

[20] Kelley, M. C. *The Earth's Ionosphere: Plasma Physics and Electrodynamics.* San Diego, California: Academic. 1989

[21] Brekke, A. *Physics of the upper polar atmosphere* Chichester, UK, Praxis Publishing, 2nd Edition 2013

[22] EISCAT Madrigal database. https://portal.eiscat.se/madrigal/

[23] Brekke A. and Moen J. The solar flux influence on quiet time conductances in the auroral ionosphere, *Geophysical research letters,* 20, 10 971-974 1993

[24] Lilensten J., Blelly P. L., Kofman W., Alcaydé. Auroral ionospheric conductivities: a comparison between experiment and modeling, and theoretical f10.7-dependent model for EISCAT and ESR. *Annales Geophysicae, European Geosciences Union* 14(12), 1297-1304 1996.

[25] Ieda A. et al Approximate forms of daytime ionospheric conductance *Journal of Geophysical Research: Space Physics 119.* 10397-10415 2014

[26] Coxon, J. C., Milan, S. E. and Anderson, B. J. (2018). A Review of Birkeland Current Research Using AMPERE. *In Electric Currents in Geospace and Beyond* (eds A. Keiling, O. Marghitu and M. Wheatland). doi:10.1002/9781119324522.ch16

[27] Anderson, B. J., Olson, C. N., Korth, H., Barnes, R. J., Waters, C. L., and Vines, S. K. (2018). Temporal and Spatial Development of Global Birkeland Currents. *Journal of Geophysical Research: Space Physics.* https://doi.org/10.1029/2018JA025254

[28] Birkeland Centre for Space Science - https://birkeland.uib.no/data/amps/

[29] University of Oslo - http://tid.uio.no/plasma/aurora/

[30] Gjerloev, J. W., Ohtani, S., Iijima, T., Anderson, B., Slavin, J., and Le, G. (2011). Characteristics of the terrestrial field-aligned current system. *Annales Geophysicae*, 29(10), 1713–1729.

[31] Lühr, H., Park, J., Gjerloev, J. W., Rauberg, J., Michaelis, I., Merayo, J. M. G., and Brauer, P. (2015). Field-aligned currents' scale analysis performed with the Swarm constellation. *Geophysical Research Letters* , 42(1), 1–8.